RADAR OBSERVATIONS OF BASALTIC LAVA FLOWS AND FISSURE VENTS: CRATERS OF THE MOON, IDAHO

by

Linda Marie Viglienzone Martel

A Thesis Presented in Partial Fulfillment
of the Requirements for the Degree
Master of Science

ARIZONA STATE UNIVERSITY

December 1984

RADAR OBSERVATIONS OF BASALTIC LAVA FLOWS AND FISSURE VENTS:

CRATERS OF THE MOON, IDAHO

by

Linda Marie Viglienzone Martel

has been approved

December 1984

APPROVED:

Paul Gierasch, Chairperson

Jonathan Fink

Michael C. Malin

Supervisory Committee

ACCEPTED:

Paul Kintner

Department Chairperson

Charles M. Bailey

Dean, Graduate College

ABSTRACT

Detection of fissure vent areas in basaltic plains using radar images requires a) characterizing surface roughness of the effused lavas and b) delineating vent structures. The utility of this approach is highly dependent on the geologic character of the particular area and on resolution constraints of the radar systems.

This study tested the hypothesis that smooth-to-rough textural transitions of effused lavas can be detected in radar images, and that these transitions occur with distance from a fissure vent.

Although smooth and rough surface textures can be successfully differentiated in X band (3-cm wavelength) and L band (25-cm wavelength) dual polarization images, there are constraints in tracing textural changes back to a particular fissure vent. First, in the Craters of the Moon lava field, near-vent shelly pahoehoe has identical backscatter to older pahoehoe with smooth mantles of aeolian material. Thus, near-vent flows do not have unique radar backscatter. Second, the stratigraphy is sufficiently complex that flows rarely can be traced to their sources. Textural transitions seen in radar images did not result from single flows emanating from fissure vents. Rather, lavas of different textures, degrees of weathering, flow paths, and source vents combined to form complex textural patterns. Small-scale, individual flows with textural transitions were not seen clearly in the radar images due to resolution restrictions of the imaging systems.

Fissure vents are detectable in the radar images by virtue of the structures that form along their lengths. Spatter ramparts paralleling

the open fissures have diagnostic, strong backscatter in the X band images. These vent structures were not delineated in the L band images. The agglutinate texture of the ramparts has an average roughness of several centimeters, which may be responsible for the appearance of the ramparts in X band, but not in L band images. Differences in system design governing resolution, such as signal to noise ratio and number of looks may also contribute to the differences in visibility of the ramparts in the radar images. The fissure vents illustrate the importance of using multiple wavelengths in radar studies.

ACKNOWLEDGEMENTS

Many thanks go to my thesis committee for providing guidance during the course of the study and for critiquing the drafts of the manuscript. I thank my advisor, Ron Greeley, for suggesting the project, providing support, and introducing me to the geology of the Snake River Plain. Mike Malin provided technical guidance while I learned radar theory and shared with me numerous thought-provoking discussions. Jon Fink graciously reviewed the manuscript and offered many helpful suggestions.

Special thanks go to Ron Blom of the Jet Propulsion Laboratory for supplying the radar images used in this study. His advice and encouragement are gratefully acknowleged. I also thank Diane Evans and Tom Farr of JPL for their continued interest in this project.

I would also like to acknowledge Charles Rosenfeld of Oregon State University and the Oregon Army National Guard 1042nd MI Company for providing radar images. Although these images were not used in the final analyses, they gave me my first "radar" views of the lava flows.

Special thanks go to Park Ranger, Neil King, and Superintendent, Robert J. Hentges of the Craters of the Moon National Monument for their cooperation and logistical help during field work in the summer of 1981. The personnel at the Idaho Falls office of the Bureau of Land Management also helped by suggesting best routes for travel over the lava flows.

My friend and colleague, Ann Lewis Edwards of University College London shared with me an exciting summer in Idaho - hiking over lava flows for my study and over sand dunes for her study. Ann's companionship, humor, and musicianship helped to keep moral high.

The hospitality and true friendship of the townsfolk of American Falls, Idaho will never be forgotten. Mr. and Mrs. Art Linscheid of the Crystal Ice Cave and Rev. and Mrs. Nixon Knight gave Ann and me a home away from home.

My husband, colleague, and best friend, Steve, through the entire course of this project, has given me the encouragement to see this through to completion. Our long discussions and brainstorming sessions always resulted in new insights. I thank him for being my sounding board and editor.

I thank my parents for their support in all my endeavors.

Special thanks go to John Bredehoeft of the U. S. Geological Survey, Menlo Park, for providing support and encouragement during the final writing stages.

From 1980 to 1982 this work was supported by grant NSG-7415 from the Office of Planetary Geology, National Aeronautics and Space Administration.

TABLE OF CONTENTS

	Page
LIST OF TABLES	viii
LIST OF FIGURES	ix
INTRODUCTION	1
PREVIOUS WORK	2
GEOLOGIC SETTING	7
RADAR THEORY	11
Synthetic Aperture Radar	12
Radar Equation	14
Simple Surface Scattering Models	18
OBSERVATIONS AND INTERPRETATIONS	23
Class 1 Lava Flows	23
Class 2 Lava Flows	43
Class 3 Lava Flows	46
Lava Textures Related to Vent Areas	49
Spatter Ramparts	51
CONCLUSIONS	56
REFERENCES CITED	58

LIST OF TABLES

page

TABLE 1. SYNTHETIC APERTURE RADAR SYSTEMS AND IMAGE DESCRIPTIONS .. 4

LIST OF FIGURES

		Page
Figure 1.	Location map of Craters of the Moon lava field, Idaho	3
Figure 2.	Map of Snake River Plain, Idaho and bordering physiographic provinces	8
Figure 3.	Geologic map of the study area, showing eruptive periods	10
Figure 4.	Sketch showing azimuth and range directions, and comparing antennas and beam widths for real and synthetic aperture radar systems	13
Figure 5.	Radar return intensity as a function of incidence angle	16
Figure 6.	Scattering patterns for three surface textures	19
Figure 7.	Derivation of Rayleigh criterion for roughness	20
Figure 8.	Derivation of Bragg resonance phenomenon	22
Figure 9.	Backscatter classes for X band, parallel polarization	24
Figure 10.	Backscatter classes for X band, cross polarization	26
Figure 11.	Backscatter classes for L band, parallel polarization	28
Figure 12.	Backscatter classes for L band, cross polarization	30
Figure 13.	Comparison of radar image and aerial photograph coverage	32
Figure 14.	Vertical aerial photograph showing flow textures of all three backscatter classes	34
Figure 15.	Vertical aerial photograph of hummocky pahoehoe lava, aa lava and smooth surfaces	36
Figure 16.	Vertical aerial photograph of flows northwest of Black Top Butte	38
Figure 17.	Vertical aerial photograph of class 2 aa lava and mixed pahoehoe-aa surfaces	40
Figure 18.	Mosaic of vertical aerial photographs of area southeast of Black Top Butte	44
Figure 19.	Vertical aerial photograph showing exposures of class 3 weathered pahoehoe	47

Page

Figure 20. Vertical aerial photograph showing a 2-km-long flow with pahoehoe-to-aa textural transition 52

Figure 21. Ground photograph of spatter ramparts 54

INTRODUCTION

Surface texture is the primary geologic element influencing radar-backscatter intensity in regionally flat, semi-arid environments. In these areas the effects of large-scale slopes and dielectric properties are inconsequential. The volcanic terrain of the eastern Snake River Plain, Idaho exemplifies such an environment. In this setting of multiple, coalescing low shields and intervening fissure flows, it is possible that textural patterns of the basaltic lava surfaces may be used to infer source-vent areas. The objective of this thesis is to examine the utility of synthetic aperture, side-looking airborne radar to detect fissure vent areas primarily by characterizing lava flow texture or surface roughness. Special attention is given to the characterization of radar backscatter from pahoehoe lava flows.

The surface texture of fresh basaltic lava flows is dependent principally on temperature, volatile content and state, viscosity, and preflow topography at the time of emplacement (Swanson, 1973; Macdonald, 1973). In the simplest cases, lavas cool and degas, becoming less glassy and more viscous with distance from the vent. The resulting systematic textural change from smooth, near-vent shelly pahoehoe to hummocky pahoehoe or aa lava may be detectable in the radar images.

Independent of lava flow textures, evidence for the location of fissure vents may be deduced from vent structures. Small-scale slope effects of open fissures or associated features such as spatter ramparts might be recognizable on the radar images.

The flows chosen for this study are part of the Craters of the Moon (COM) lava field in the eastern Snake River Plain of Idaho (Fig. 1). They are associated with eruptive fissures of the Great Rift (Prinz, 1970) and represent one of the largest accumulations of Holocene basaltic lava in the conterminous United States. This terrain exhibits a classic plains volcanism style (Greeley, 1982) and was chosen for study because of the wide range in morphologies of the flows.

Systematic textural changes and/or vent structures are located on the basis of backscatter information provided by four radar images. These images were acquired from X band (3-cm wavelength) and L band (25-cm wavelength) synthetic aperture radar systems (Table 1). The working hypothesis is that changes from smooth to rough lava textures with distance from a fissure vent produce changes in backscatter intensities that will be manifest as systematic changes in gray tones on the radar images. Moreover, open fissure vents or vent structures may provide unique backscatter signatures.

Radar theory and scattering models aid in the interpretation of backscatter intensity. Geologic maps (Kuntz and others, 1983), aerial photographs, and field observations provide verification of surface roughness, flow directions, and possible vent locations.

PREVIOUS WORK

Previous radar studies of volcanic terrains have discriminated between surface morphologies of lava flows based on relative backscatter differences. A common objective has been to assess the relationship between surface roughness and backscatter intensity at the operating

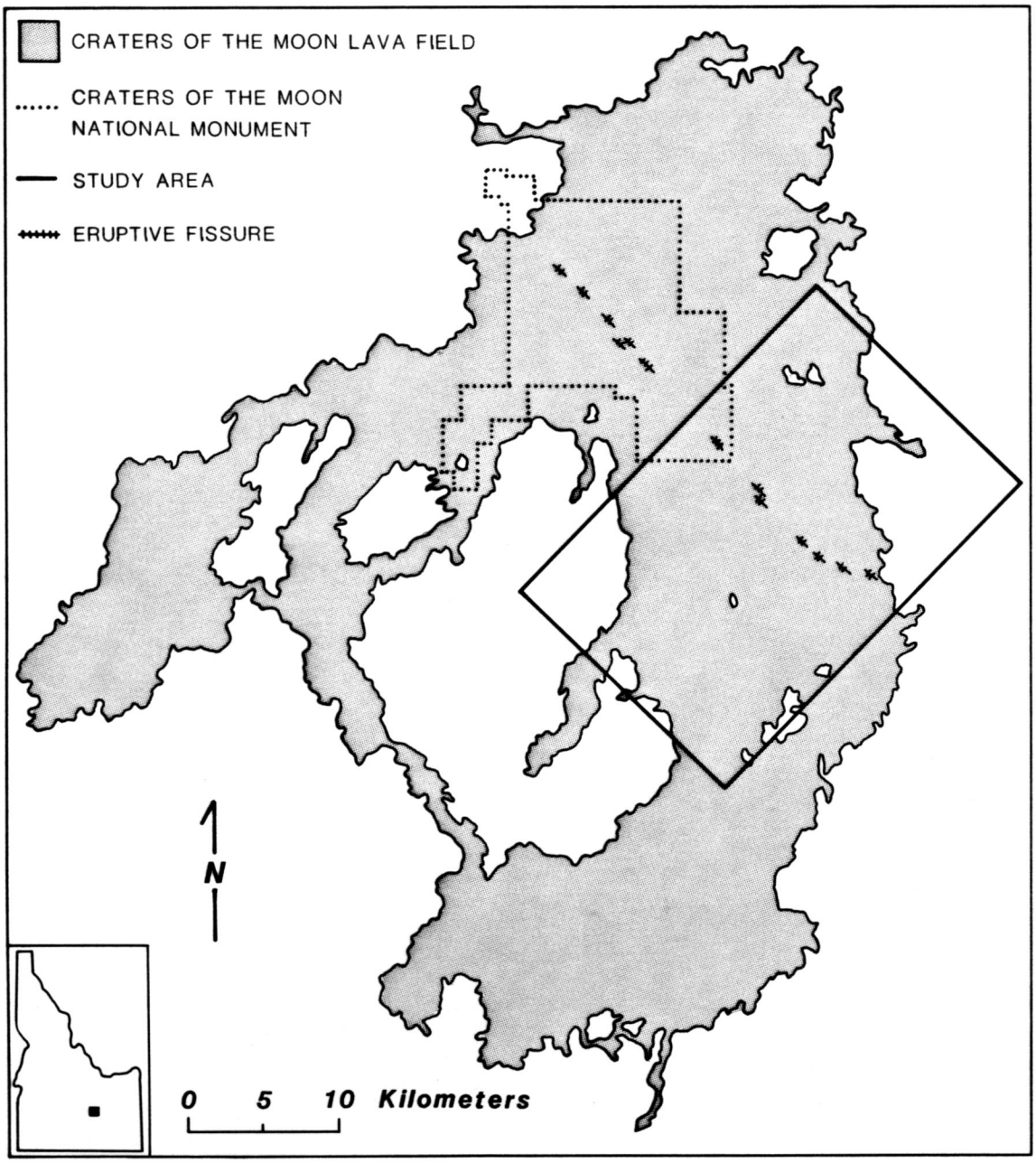


Figure 1. Location map of Craters of the Moon lava field, Idaho showing study area.

TABLE 1. SYNTHETIC APERTURE RADAR SYSTEMS AND IMAGE DESCRIPTIONS

	X band system	L band system
Wavelength; frequency	3 cm; 9600 MHz	25 cm; 1.2 GHz
Incidence angle	45° to 65°	0° to 40°
Polarization	HH, HV	HH, HV
Look direction	N 45° W	N 35° W
Resoltion cell (azimuth x range)	15 x 15 m	30 x 10 m
Source	Johnson Space Center	Jet Propulsion Laboratory
Dates of acquisition	July, August 1981	August, September 1977

wavelengths and polarizations. Ka (0.83 cm), C (6.73 cm), and P band (70.0 cm wavelength) images were used at Pisgah lava field to evaluate the wavelength dependence of backscatter intensity by Dellwig and Moore (1966) and Dellwig (1969). Generally, they found that discrimination between lava textures was difficult with the shorter wavelength radar systems and that subsurface penetration of the long wavelength radar could influence backscatter intensity.

Using K (0.86 cm), X (3.0 cm), L band (25.0 cm) and Seasat (23.5 cm wavelength) data for the Pisgah lava field, Elachi and others (1980) successfully distinguished pahoehoe from aa lavas only in the Seasat and cross-polarized airborne images. The parallel-polarized images had uniform tone for both textures. Elachi and others (1980) concluded that the backscatter intensity of the aa lava was sensitive to polarization. A second important finding was that two pahoehoe units from separate eruptive phases were indistinguishable in all images although one surface was more hummocky with pressure ridges, lava tubes and tumuli than the other pahoehoe surface.

L band, computer-enhanced images were used by Malin and others (1978) and Evans (1978) to examine the surface roughness of the ash, pumice, and aa lava flow units of Askja Caldera, Iceland. The consistently strong backscatter from aa lava flows with surface roughness ranging from centimeters to several meters was attributed primarily to the extreme roughness of the surface. However, it was further noted that the water content of lichen could have raised the dielectric constant of the aa, thereby contributing to the observed high reflectivity.

SP lava flow in Arizona was studied using K, X, and L band images (Schaber and others, 1980). Two lava-surface types were identified on

the basis of tonal differences in the L band image. These surface types are a blocky basaltic andesite lava flow and lava flows subdued by tephra deposits and vegetation. Schaber and others (1980) explained the lack of relative tonal difference in the K band and X band images by showing that the mean relief of both surface types exceeded the Rayleigh criterion for smoothness; hence, the surfaces appeared indistinguishably rough in the shorter-wavelength images.

Backscatter variations of two basaltic aa flows and a blocky dacitic flow in Medicine Lake Highland, California were studied using airborne L band radar and Seasat images (Elachi and others, 1980; Farr and others, 1981). Again, rough, craggy surfaces produced the effect of strong backscatter.

Backscatter variations of the basaltic lava flows in the eastern Snake River Plain, Idaho were first described by Daily and others (1979) and Elachi and others (1980). Only dual-polarization, airborne L band and Seasat images were available. In general, the Pleistocene pahoehoe lavas, commonly smoothed by loess and soil covers, displayed weaker backscatter than the unmantled Holocene pahoehoe and aa lavas. In the Craters of the Moon (COM) lava field, as elsewhere, the aa lavas showed the strongest radar backscatter.

Most of these previous radar studies of lava flows involved aa and block lava textures. This investigation of the COM lava field provides the first detailed radar study of extensive pahoehoe lava flows.

GEOLOGIC SETTING

The Snake River Plain is an arcuate, topographic depression spanning 650 km of southern Idaho from the Idaho-Oregon border eastward to the Yellowstone Plateau (Fig. 2). It is composed chiefly of Quaternary basaltic rocks, aeolian sand and loess, and minor outcrops of silicic volcanic rocks and gravel. The Idaho Batholith and the Northern Rocky Mountain Province bound the plain to the north. To the south it is bounded by the Owyhee Mountains and by the Basin and Range Province.

The Snake River Plain east of 114° longitude consists predominantly of two forms of basaltic lavas: fissure-fed flows associated with aligned vents, and low shields (Greeley, 1982). The largest field of compound fissure-fed flows, and the subject of this study, is the Craters of the Moon (COM) lava field. It is aligned along a N 35° W-trending set of fissure vents, spatter cones, and cinder cones defining the Great Rift of the Idaho Rift System (Prinz, 1970). Most of the vents lie within and to the southeast of the COM National Monument. The flows comprise units of the upper part of the Snake River Group of late Pleistocene and Holocene age. The lavas are olivine tholeiites and alkali olivine basalts (Stone, 1967; Leeman and others, 1976; Stout and Nicholls, 1977).

Kuntz and others (1983) estimated that more than forty lava flows erupted from more than eight fissure vents and twenty-five cinder cones to form the COM lava field. Based on field, radiocarbon, and paleomagnetic data, they determined that the COM lava field formed during the last 15,000 years in at least eight eruptive periods, each lasting no more than 1,000 years.

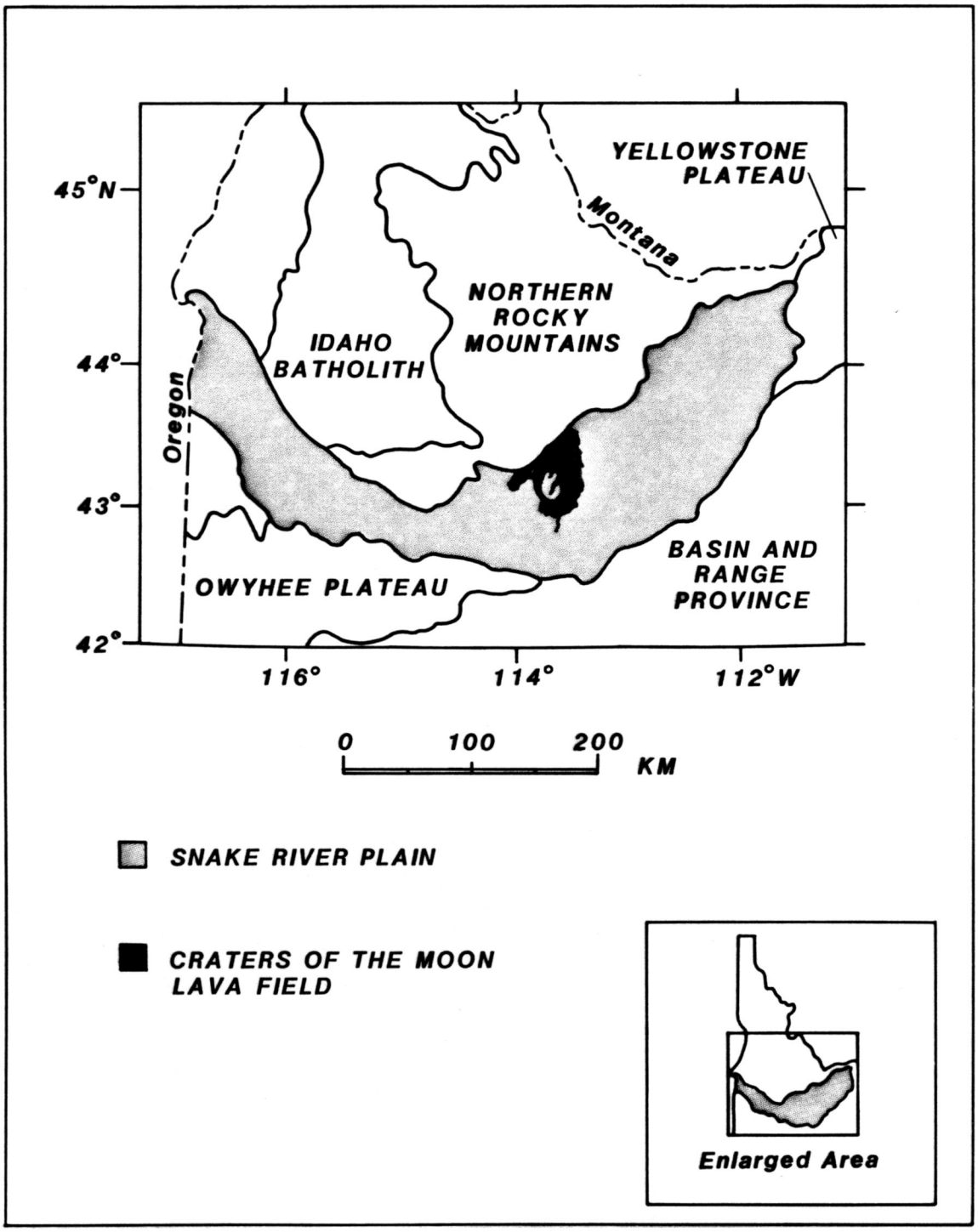


Figure 2. Map of Snake River Plain, Idaho and bordering physiographic provinces (after Kuntz and others, 1983).

Six of the eight eruptive periods are represented in the 500 km^2 study area located southeast of the COM National Monument (Fig. 3). The flows and their approximate ages were described by Kuntz and others (1983) as follows:

(1) Qba - 2,100 to 2,300 years B.P., chiefly pahoehoe and lesser amounts of aa lava erupted from fissures along the Great Rift in the COM National Monument;

(2) Qbb - 3,500 to 4,500 years B.P., shelly, slabby, and hummocky pahoehoe lava erupted chiefly from fissures along the Great Rift near Blacktop Butte;

(3) Qbc - 5,800 to 6,200 years B.P., bulbous aa lobes from Big Cinder Butte cinder cone and an earlier sequence of fissure-fed pahoehoe lava flows which show transition to aa lava with distance from the vents;

(4) Qbd - 6,600 years B.P., not represented in study area, bulbous aa lobes erupted from Silent Cone cinder cone;

(5) Qbe - 7,300 to 7,900 years B.P., bulbous aa lobe with 25 m high flow fronts;

(6) Qbf - 10,000 to 11,000 years B.P., pahoehoe lava flows with probable source vents along Great Rift near Sheep Trail Butte and Crescent Butte;

(7) Qbg - 12,000 to 12,900 years B.P., not represented in study area, pahoehoe and aa lava from Sunset Cone cinder cone;

(8) Qbh - 15,000 years B.P., pahoehoe lava flows with no known source vents.

These flows are underlain by Pleistocene (>15,000 years B.P.) basaltic lava flows of the lower part of the Snake River Group, map unit Qbs.

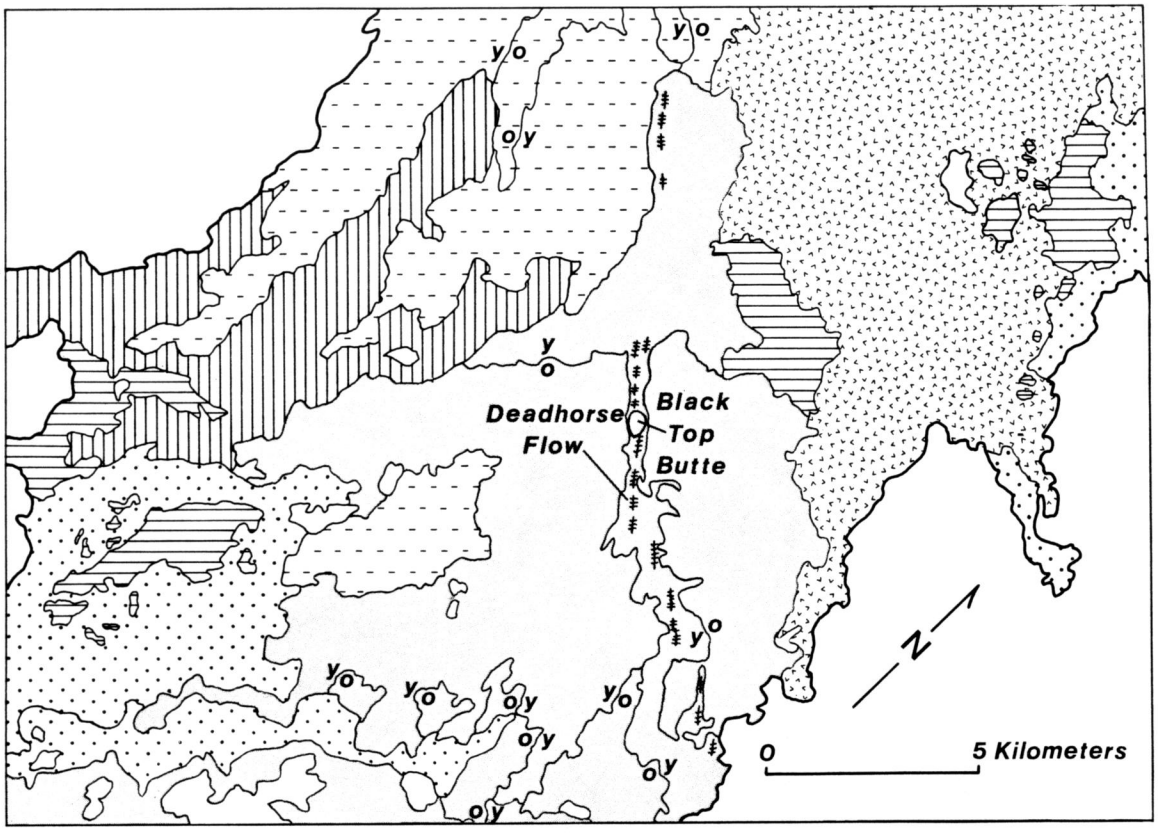


Figure 3. Geologic map of the study area, showing eruptive periods (from Kuntz and others, 1983).

Flows of the Qbs unit are chiefly pahoehoe lava with minor components of aa lava, cinders, and ash. Aeolian deposits ranging in thickness from less than 1 m to 3 m characteristically cover the surfaces of Qbs lava flows. Map units from Kuntz and others (1983) are used in this thesis.

RADAR THEORY

Active, monostatic, side-looking airborne radar is an imaging system that transmits and receives microwave energy from the same location. Passive systems, such as microwave radiometers, thermal infrared sensors, and visible sensors receive, but do not transmit, radiation.

A radar image is a two dimensional record of the microwave energy scattered or reflected from the ground back to the antenna. The intensity of this returned energy, a function of both the radar system parameters and terrain characteristics, appears as grey tones on radar images.

This section begins with a discussion of synthetic aperture, side-looking airborne radar and the processes that transform the received radar signals into an image (Ulaby and others, 1982). The radar equation, which relates backscatter intensity to the radar system parameters and terrain characteristics, is introduced next (Fung and Ulaby, 1983). The section ends with the criteria for roughness established by the Rayleigh and Bragg scattering models (Beckmann and Spizzichino, 1963; Ulaby and others, 1982).

Synthetic Aperture Radar

Synthetic aperture radar systems use signal storage and processing techniques to improve resolution beyond that achieved by real aperture systems. The resolution of imaging radars, real and synthetic aperture, is defined for two directions (Fig. 4), azimuth (parallel to ground track), and range (perpendicular to ground track). Storing and processing radar signals enables the synthetic aperture system to simulate a much longer antenna than is used. A longer antenna improves azimuth resolution by narrowing the effective width of the fan-shaped beam (Fig. 4). Range resolution is improved with time-delay measurements of the returned radar signals. Together, azimuth and range resolutions define the resolution cell, that is, that portion of the ground resolved as a unique scattering area.

High resolution is achieved by synthetic aperture radar systems by storing and summing multiple reflected signals from the ground along the flight path. Synthetic aperture systems detect and preserve the Doppler shifts in waveforms resulting from the apparent motion of the ground target relative to the radar antenna. For example, when the leading edge of an incident wave with known frequency strikes an arbitrary point on the ground, A, the backscattered signal is shifted to a slightly higher frequency. No frequency shift occurs when the incident wave is centered on point A. When the trailing edge of the incident wave strikes point A the backscattered signal is shifted to a slightly lower frequency. Doppler shifts, amplitudes of the backscattered waveforms, and time-delay information are stored as synchronized intensity-modulated light spots on photographic film, as described below, or on

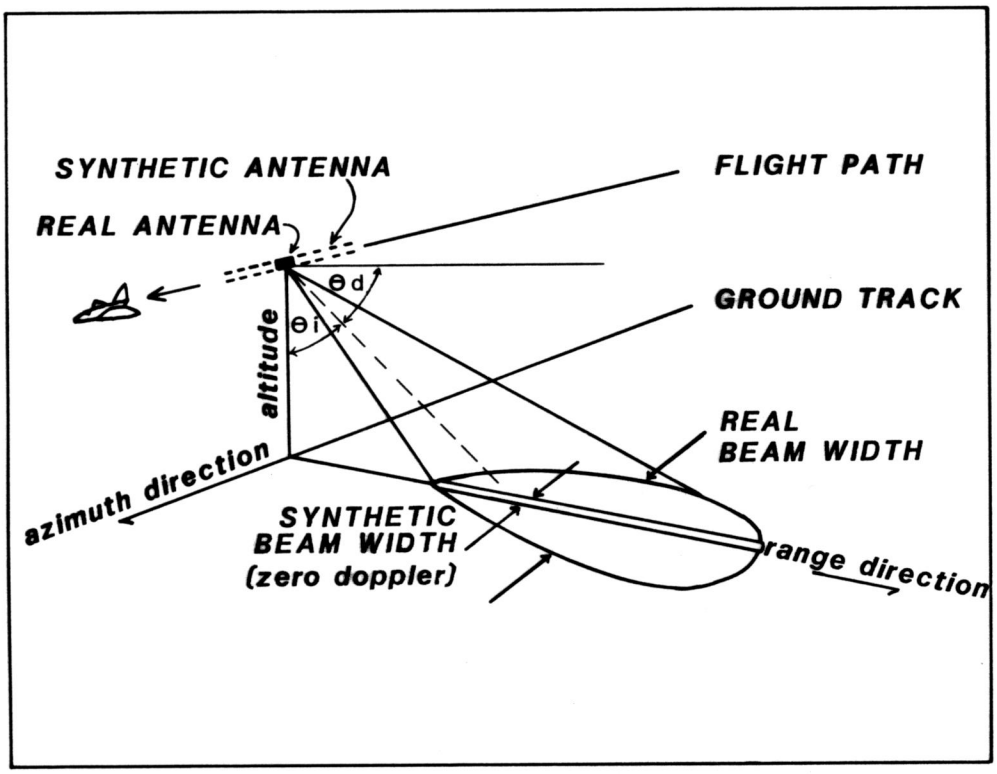


Figure 4. Sketch showing azimuth and range directions, and comparing antennas and beam widths for real and synthetic aperture radar systems. Θi is incidence angle and Θd is depression angle.

magnetic tape for a digital display. The information is stored for later processing.

During processing, each transmitted and received signal is compared with a coherent reference signal to produce an interference pattern. Constructive interference results in a bright spot on a cathode ray tube (CRT), whereas destructive interference produces a dark spot. The interference patterns of successive returns from point A appear as a broken line across the CRT. This broken line, termed the signal history of point A, is transferred onto a strip of film moving at a velocity proportional to the velocity of the aircraft, to yield a radar hologram. A coherent light diffracted through the hologram, in an optical correlator, creates a sharp, unique image point representing the original point A.

Hence, the motion of the antenna relative to the ground allows successive returns from point A to be processed into a final image point. The antenna functions as though its physical length were equivalent to the entire distance between the initial and final waves striking point A. The received microwave signals are processed for all the points along a flight line to produce a radar image.

Radar Equation

The interpretation of a radar image requires a knowledge of how radar waves are reflected and scattered by the terrain. The radar equation describes the power received by the antenna in terms of system parameters and terrain characteristics (Fung and Ulaby, 1983):

$$P_{ar} = \frac{P_t \, G^2 \, \lambda^2 \, \sigma^o{}_{rt}}{(4\pi)^3 \, R^4} \qquad (1)$$

where P_{ar} is the average received power, P_t is transmitted power, G is the gain of the antenna in the direction of the target, λ is radar wavelength, R is the distance between the radar and ground target, and $\sigma^o{}_{rt}$ is the average differential cross-section or scattering coefficient. P_t G, and λ are constants of the radar system and R commonly is known. Significantly, when these parameters are held constant, P_{ar} varies only with $\sigma^o{}_{rt}$. The scattering coefficient applies to targets much larger than the resolution cell of the radar system and represents the integrated backscatter from multiple scatterers. The magnitude of the scattering coefficient is a function of incidence angle, slope, polarization, dielectric properties of the material, wavelength, and surface roughness.

Incidence angle and slope define the orientation of an incident radar wave relative to the terrain. Incidence angle is the angle between a transmitted radar wave and the surface normal; in the special case of a flat surface, incidence angle equals 90° minus depression angle. Maximum radar return results when incidence angle is 0°. Minimum return results where the incoming radar waves graze the surface. As incidence angle increases, radar-return intensity generally decreases rapidly for smooth surfaces and slowly for rough surfaces (Fig. 5).

Polarization of an electromagnetic wave describes the orientation of the electric-field vector at a given point in space during one period of oscillation (Long, 1975). The imaging radar systems used in this

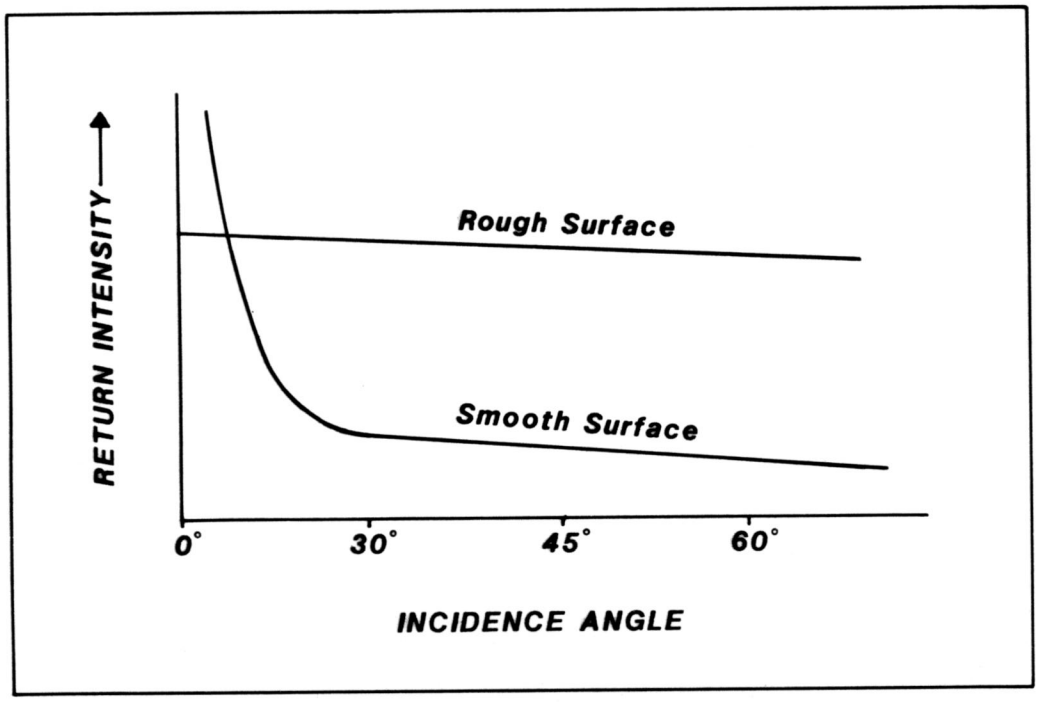


Figure 5. Radar return intensity as a function of incidence angle for two surface textures (after Sabins, 1978).

thesis are capable of parallel- and cross-polarized configurations. In parallel polarization (HH) transmitted and received electric-field vectors are horizontal. A physical process responsible for the parallel polarized return is quasi-specular reflection from flat surfaces oriented normal to the incoming waves. Another process is direct surface scattering off slightly rough surfaces (Janza, 1975; Fung and Ulaby, 1983). In cross polarization (HV), also called depolarization, transmitted electric-field vectors are horizontal but received electric-field vectors are vertical. Radar waves are depolarized primarily by multiple surface scattering, double bounce, or multiple volume scattering (Janza, 1975; Fung and Ulaby, 1983). Volume scattering applies to the subsurface penetration of radar waves into inhomogeneous material. Some of the waves scattered within the volume of material may exit the surface and contribute to the overall signal received back at the antenna (Ulaby and others, 1982).

The complex dielectric constant of a material varies with temperature, frequency of the impinging energy, and chemistry, and is highly influenced by water content. A large dielectric constant increases the reflectivity of a surface which results in stronger returned signals and reduced subsurface penetration.

The wavelength of incident radar energy helps to define the effective surface roughness. That is, a surface may appear to be smooth or rough depending on radar wavelength, incidence angle, horizontal spacing of surface roughness elements, and the standard deviation of surface height variation, refered to as the root mean square (rms) surface height. For rms surface height less than the radar wavelength, radar-return intensity is minimized because of the dominance of specular

reflection away from the radar antenna. The surface will appear smooth or only slightly rough (Fig. 6a). Specular reflection at normal incidence is a special case. This is the only situation for which specular reflection will produce a strong return. As this situation is not common, a strong return generally indicates diffuse scattering from a rough surface. As rms surface height increases, diffuse scattering becomes more important (Fig. 6b). For rms surface height much greater than the radar wavelength, scatter can be nearly isopropic and the surface will appear rough (Fig. 6c).

Simple Surface Scattering Models

The Rayleigh criterion (Fig. 7) establishes a simple, qualitative division between smooth and rough surfaces using radar wavelength and incidence angle. The criterion is derived from the phase difference ($\Delta\phi$) of two radar waves reflected off a slightly rough surface (Beckmann and Spizzichino, 1963). A phase difference of zero implies phase addition; the surface reflects specularly and is smooth. A phase difference equal to π implies phase opposition, where two rays interfere to the extent of cancelling each other in the direction of propagation. Hence, the energy must be redistributed in other directions, for it cannot be lost. Therefore, for $\Delta\phi = \pi$ the surface scatters diffusely and is rough. A phase difference equal to $\pi/2$, the mid-way point, is the arbitrary division between smooth and rough surfaces chosen by Rayleigh (Beckmann and Spizzichino, 1963). The phase difference of $\pi/2$ is most commonly used, although $\pi/4$ and $\pi/8$ have also been suggested (Beckmann and Spizzichino, 1963; Ulaby and others, 1982). Hence, the Rayleigh

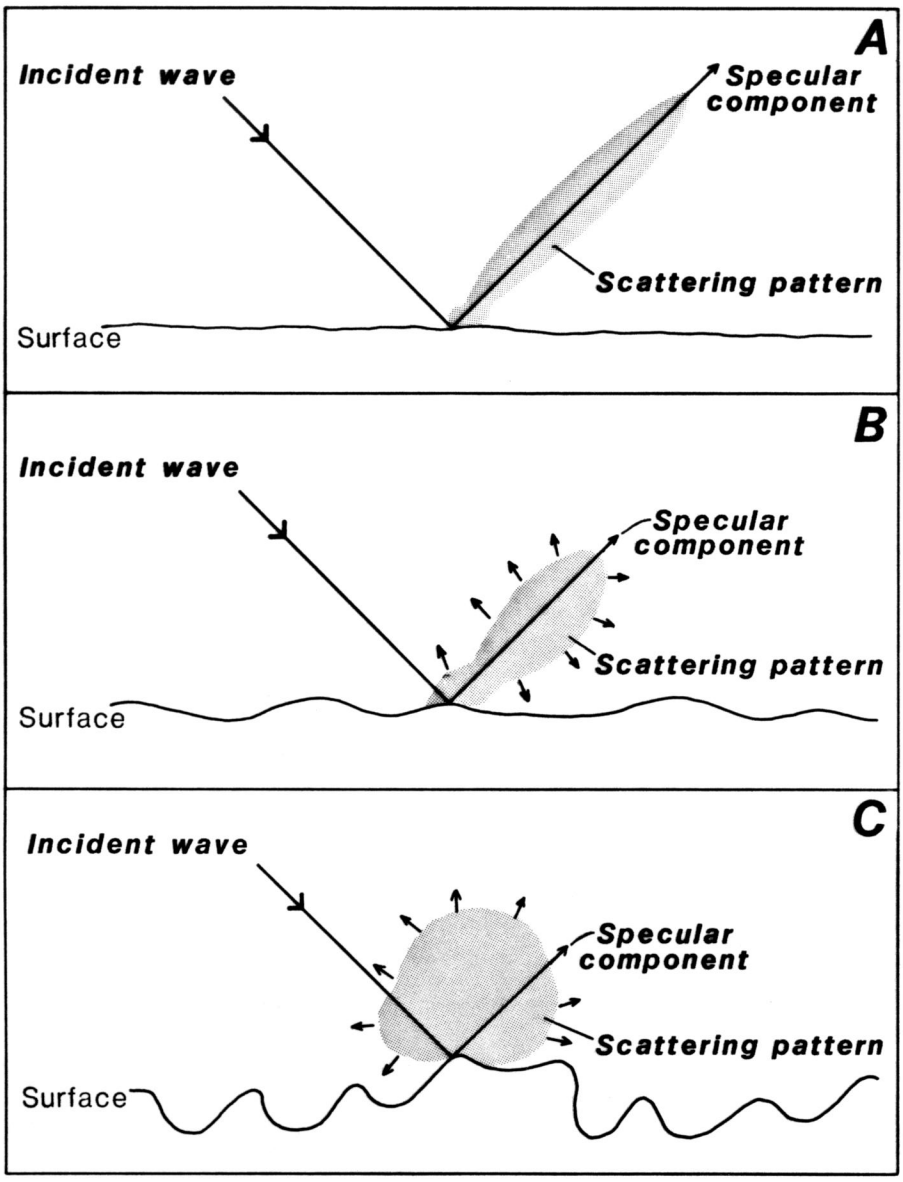
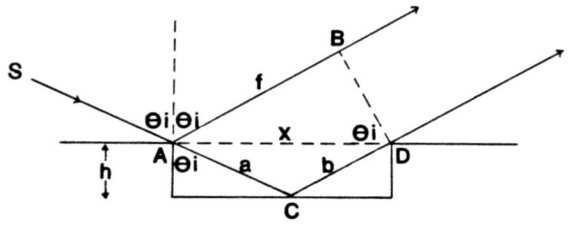


Figure 6. Scattering patterns for three surface textures: (A) smooth surface, specular reflection component dominates pattern, backscatter is negligible; (B) slightly rough surface, specular component is smaller, diffuse scattering component has grown, backscatter increases; (C) rough surface, pattern consists of only diffuse scattering, the specular component is negligible, backscatter is strong (from Ulaby and others, 1982).



2 rays

θi = incidence angle
h = rms surface height

Path length difference = ΔP = (S-A-B) - (S-C-D)
= a + b - f

$$a = b = \frac{h}{\cos\theta i} \qquad \Delta P = \frac{2h}{\cos\theta i} - f$$

$x = 2h \tan\theta i$ and $f = x \sin\theta i$ $\qquad f = 2h \tan\theta i \sin\theta i$

$$\Delta P = \frac{2h}{\cos\theta i} - 2h \tan\theta i \sin\theta i = \frac{2h}{\cos\theta i} - \frac{2h}{\cos\theta i} (\sin^2\theta i)$$

$$= \frac{2h}{\cos\theta i} (1 - \sin^2\theta i) = \frac{2h}{\cos\theta i} (\cos^2\theta i) =$$

$$\Delta P = 2h \cos\theta i$$

$$\Delta\phi = \text{phase difference} = \frac{2\pi}{\lambda}(2h \cos\theta i)$$

For $\Delta\phi = 0$, specular reflection

For $\Delta\phi = \pi$, totally rough (Lambertian surface)

For $\Delta\phi = \frac{\pi}{2}$, simple criterion for roughness (the simple half-way point)

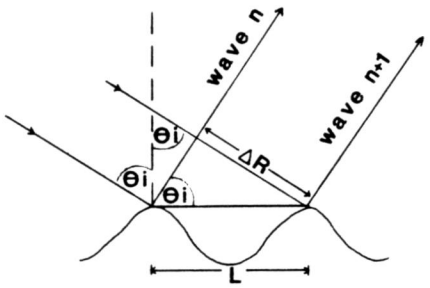
$$\frac{\pi}{2} = \frac{2\pi}{\lambda}(2h \cos\theta i)$$

$$\boxed{h = \frac{\lambda}{8 \cos\theta i}}$$

Figure 7. Derivation of Rayleigh criterion for roughness.

criterion (Fig. 7) is used to find the rms surface height, h, that theoretically represents a transition between smooth and rough surfaces for a given radar wavelength and incidence angle.

The Bragg resonance effect (Fig. 8) describes the strong radar return produced by the in-phase sum of individual waves scattered from a rough surface. For a given radar wavelength and incidence angle, a unique spatial wavelength, L, satisfies the Bragg condition resulting in a bright return. Parallel-polarized returns appear to be sensitive to this spacial wavelength whereas cross-polarized returns may be more indicative of an average roughness (Daily and others, 1978).



θi = incidence angle
L = spacial wavelength
Δ R = Lsinθi = distance between waveforms
λ = radar wavelength

A slightly rough surface is modeled as a sinusoidal surface. If the excess distance from the source to each successive wave crest is $\lambda/2$, the round-trip phase difference between the return signals from successive crests is 360°, so the signals add in phase (Ulaby and others, 1982).

In terms of the spatial wavelength, L, and the incidence angle, θi, the Bragg resonance condition is derived as follows:

$\Delta R = \frac{2\pi}{\lambda} \Delta R = n\pi$, where n is an integral multiplier and where $\frac{2\pi}{\lambda} \Delta R$ is the phase difference

$\Delta R = L\sin\theta i$ (from figure)

$\Delta R = \frac{2\pi}{\lambda}(L\sin\theta i) = n\pi$, solving for L:

$$\boxed{L = \frac{\lambda}{2\sin\theta i}}$$

ΔR is a function of λ; hence, both of these paramenters are constants of the radar system. θi is also a constant. Therefore, there is one unique L that satisfies the resonance condition.

Figure 8. Derivation of Bragg resonance phenomenon.

OBSERVATIONS AND INTERPRETATIONS

Three major classes of lava flows can be identified in the radar images of the Craters of the Moon (COM) lava field (Figs. 9-13). The backscatter characteristics of these lava flows are the following:

Class 1: strong but variable (bright, mottled tones) in all four images;

Class 2: multiple intensities - strong (bright) in XHH, weak (dark) in XHV, strong but variable (bright, mottled) in LHH, and very strong (very bright tones) in LHV;

Class 3: weak (dark tones) in all four images.

Class 1 lava flows cover most of the COM lava field and compose the background against which class 2 and 3 lava flows are set. Class 2 lava flows are scattered throughout the lava field. Class 3 flows occur in several locations, most notably along fissure vents.

Class 1 Lava Flows

The bright, mottled tones in all four images for class 1 flows suggest that the surfaces are sufficiently rough to cause scattering at both radar wavelengths. The Rayleigh criteria for roughness (Fig. 7) are rms surface heights greater than approximately 1 cm at X band and 3 cm at L band wavelengths.

Hummocky pahoehoe (Figs. 14, 15) and mixed pahoehoe-aa surfaces (Figs. 16, 17) are the dominant textures with class 1 backscatter characteristics. Field observations by the author show that the hummocky pahoehoe flows are characterized by ropy surfaces, an assortment of

Figure 9. Backscatter classes for X band, 3-cm wavelength radar with parallel polarization: (A) XHH radar image; (B) map of backscatter classes compiled from all four radar images. In this map, contacts are based on backscatter differences; dashes mark intra-unit contacts of subtle backscatter changes. Class 1 and class 2 flows have bright tones. Class 3 flows have dark tones. The barbed lines denote the locations of eruptive fissures as determined from the geologic map by Kuntz and others (1983).

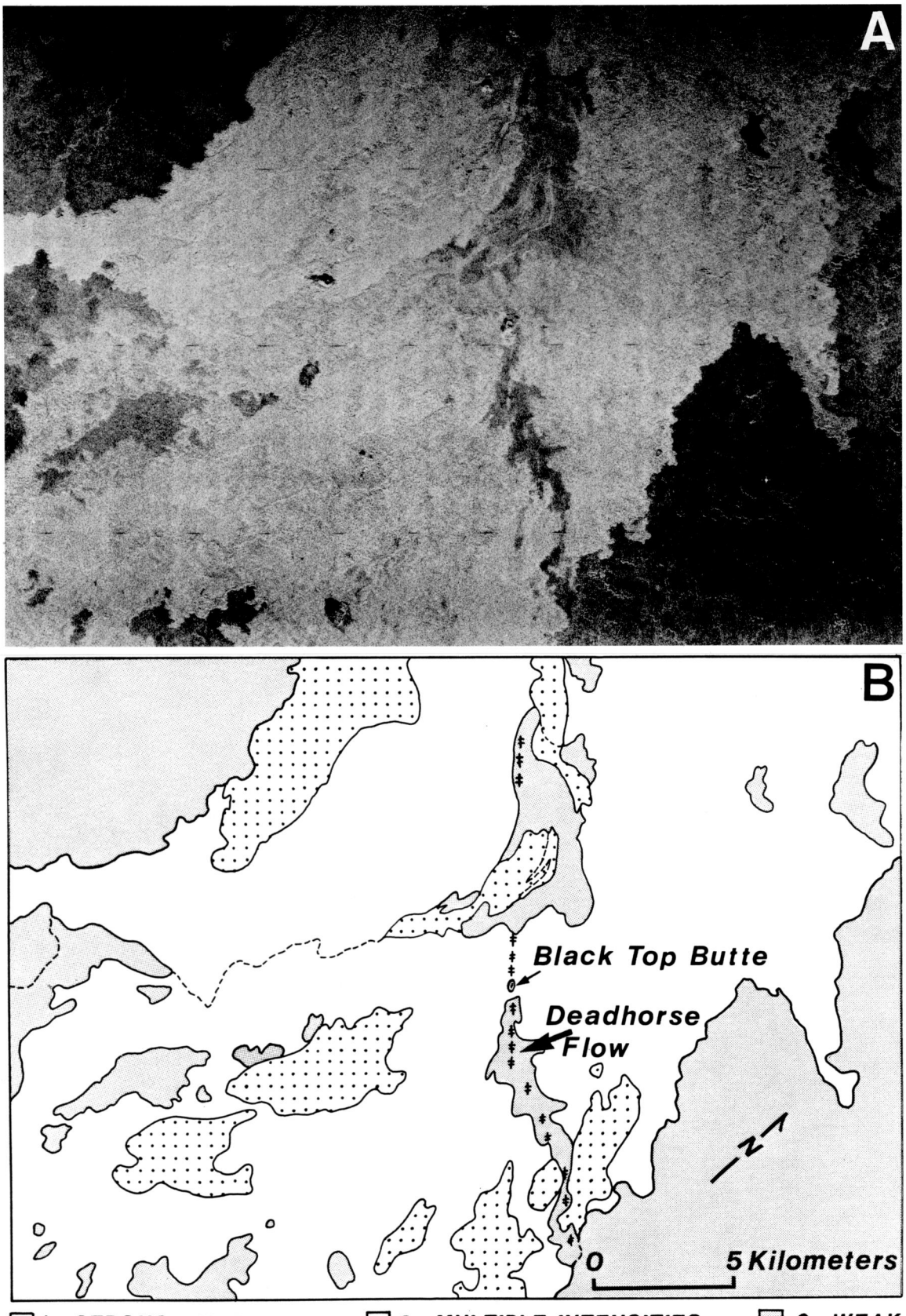

A
B
Black Top Butte
Deadhorse
Flow
N
0
5 Kilometers
1: STRONG , VARIABLE
2: MULTIPLE INTENSITIES
3: WEAK

Figure 10. Backscatter classes for X band, 3-cm wavelength radar with cross polarization: (A) XHV radar image; (B) map of backscatter classes compiled from all four radar images. In this map, contacts are based on backscatter differences; dashes mark intra-unit contacts of subtle backscatter changes. Class 1 flows have bright, mottled tones. Class 2 flows have dark tones. Class 3 flows have dark tones. The barbed lines denote the locations of eruptive fissures as determined from the geologic map by Kuntz and others (1983).

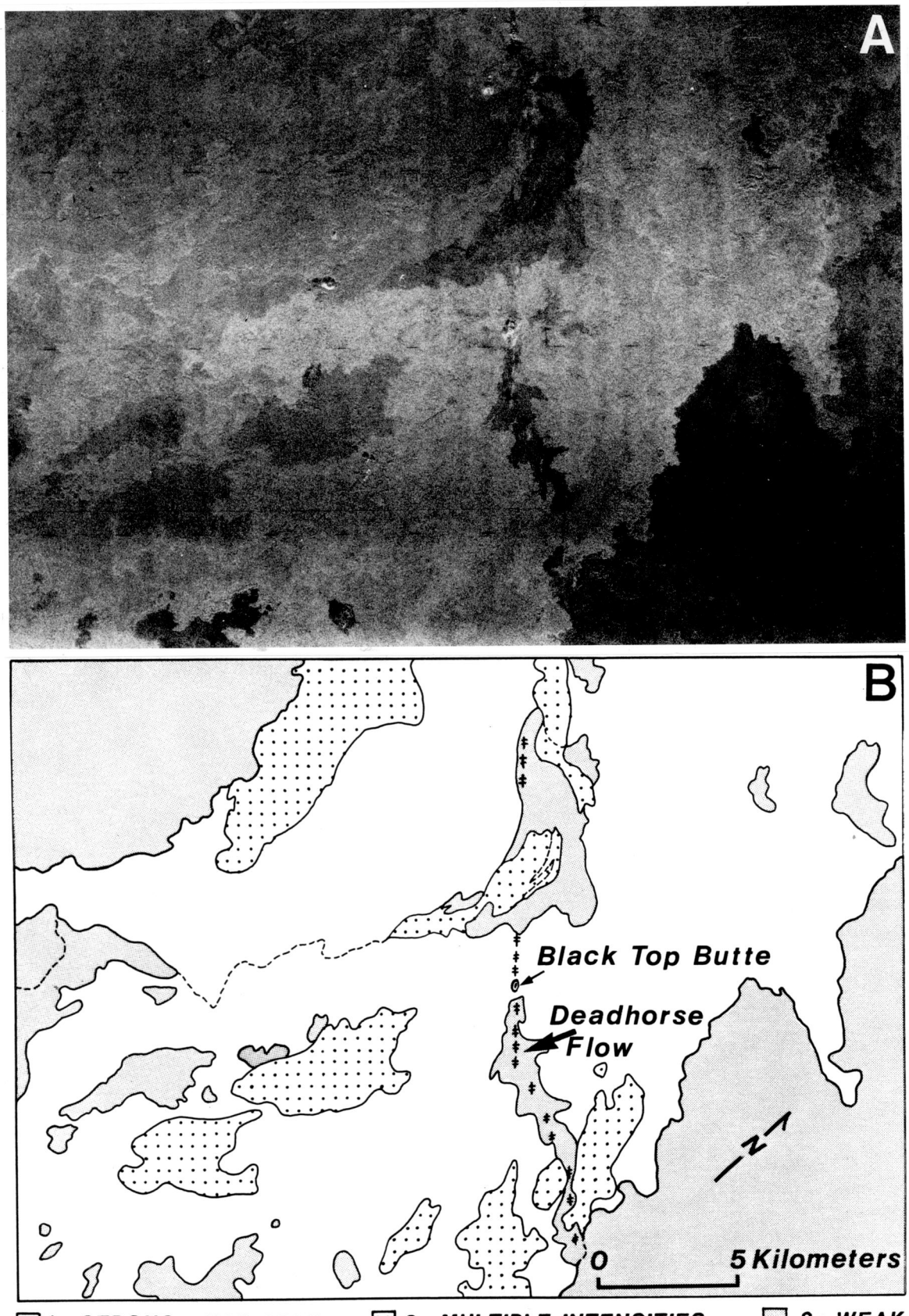

A
B
Black Top Butte
Deadhorse
Flow
N
0
5 Kilometers
1: STRONG , VARIABLE
2: MULTIPLE INTENSITIES
3: WEAK

Figure 11. Backscatter classes for L band, 25-cm wavelength radar with parallel polarization: (A) LHH radar image; (B) map of backscatter classes compiled from all four radar images. In this map, contacts are based on backscatter differences; dashes mark intra-unit contacts of subtle backscatter changes. Class 1 flows have bright tones. Class 2 flows have bright, mottled tones. Class 3 flows have dark tones. The barbed lines denote the locations of eruptive fissures as determined from the geologic map by Kuntz and others (1983).

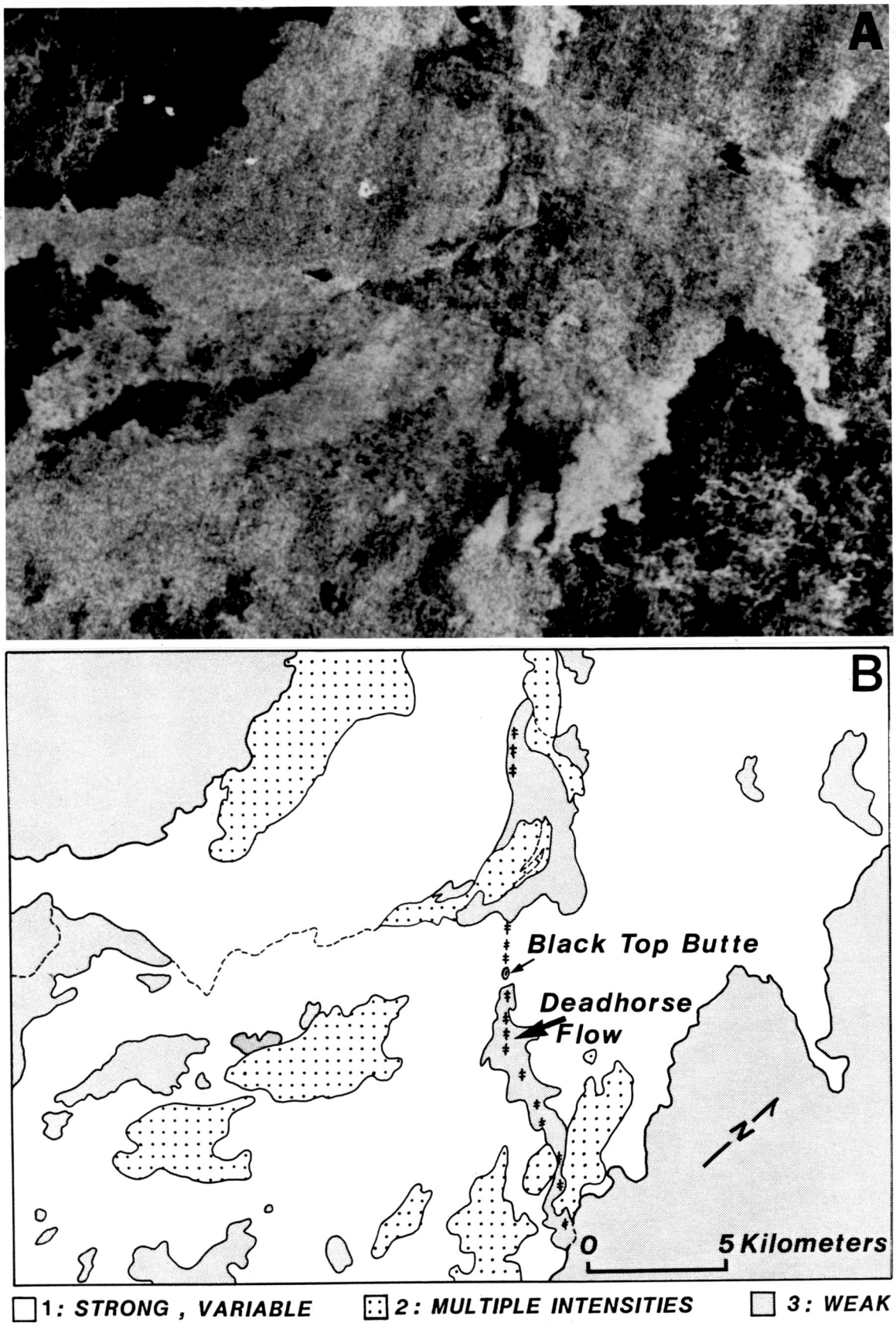

A
B
Black Top Butte
Deadhorse
Flow
N
0
5 Kilometers
1: STRONG , VARIABLE
2: MULTIPLE INTENSITIES
3: WEAK

Figure 12. Backscatter classes for L band, 25-cm wavelength radar with cross polarization: (A) LHV radar image, the two dark bands are artifacts of a mosaicking process and they contain no backscatter information. The two small arrows indicate flows with textural transitions (see text, p. 51); (B) map of backscatter classes compiled from all four radar images. In this map, contacts are based on backscatter differences; dashes mark intra-unit contacts of subtle backscatter changes. Class 1 flows have bright tones. Class 2 flows have very bright tones. Class 3 flows have dark tones. The barbed lines denote the locations of eruptive fissures as determined from the geologic map by Kuntz and others (1983).

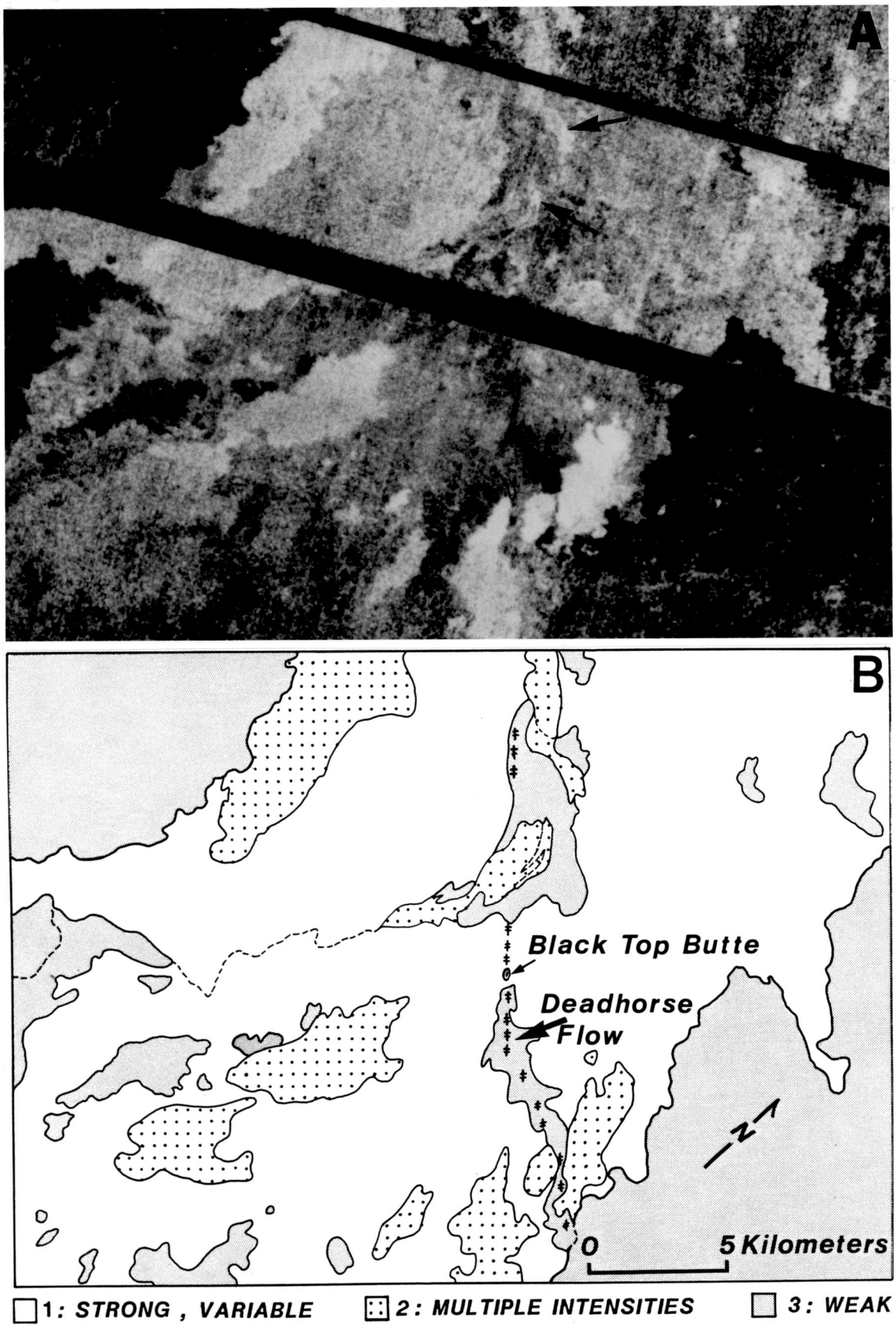
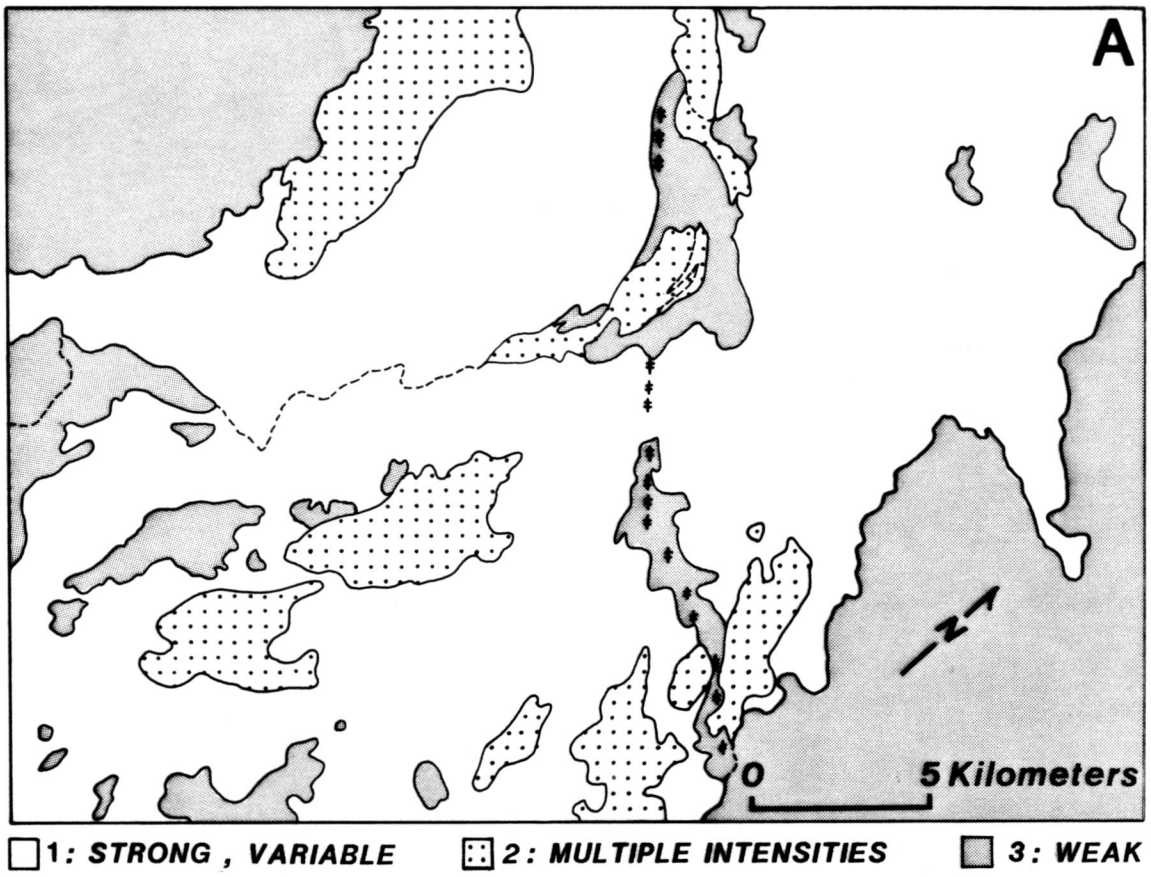

A
B
Black Top Butte
Deadhorse
Flow
N
0
5 Kilometers
1: STRONG , VARIABLE
2: MULTIPLE INTENSITIES
3: WEAK

Figure 13. Comparison of radar image and aerial photograph coverage: (A) radar backscatter compilation map; (B) same map showing locations of Black Top Butte, the Deadhorse flow, and locations of aerial photographs used in this section.


A
N
0
5 Kilometers
1: STRONG , VARIABLE
2: MULTIPLE INTENSITIES
3: WEAK

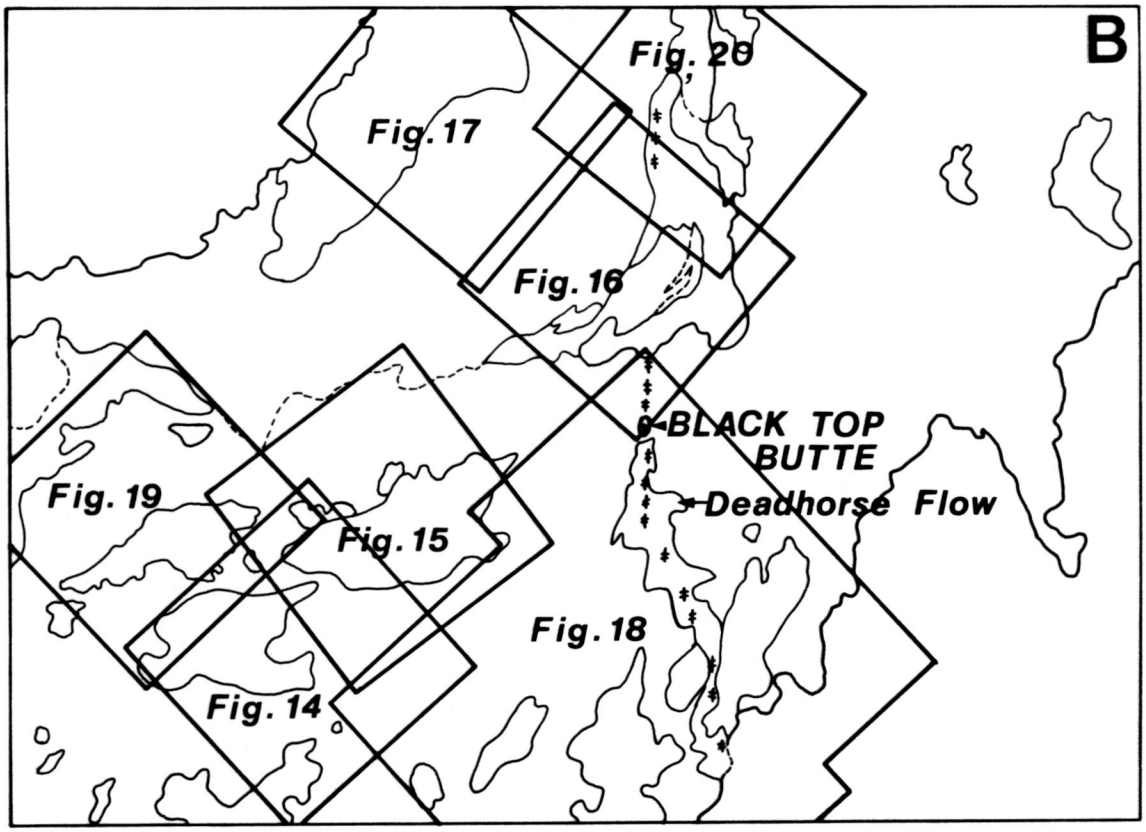

B
Fig. 20
Fig. 17
Fig. 16
BLACK TOP BUTTE
Deadhorse Flow
Fig. 19
Fig. 15
Fig. 18
Fig. 14

Figure 14. Vertical aerial photograph showing flow textures of all three backscatter classes. Class 1 hummocky pahoehoe flows have medium gray tones (1). Note pressure plateaus with collapse pits near flow margin (black arrows). Class 2 aa flows have the darkest gray tones (2). Flow direction can be deduced from internal streak patterns parallel to flow direction and ribbed patterns perpendicular to flow (white arrows). Class 3 smooth pahoehoe lava covered with windblown sediments have the brightest tones (3). These are kipukas of Pleistocene lava.
See Figure 13 for locations of the contacts between backscatter classes.
U.S. Geological Survey photograph, GS SWEZ 6-146, September, 1971.

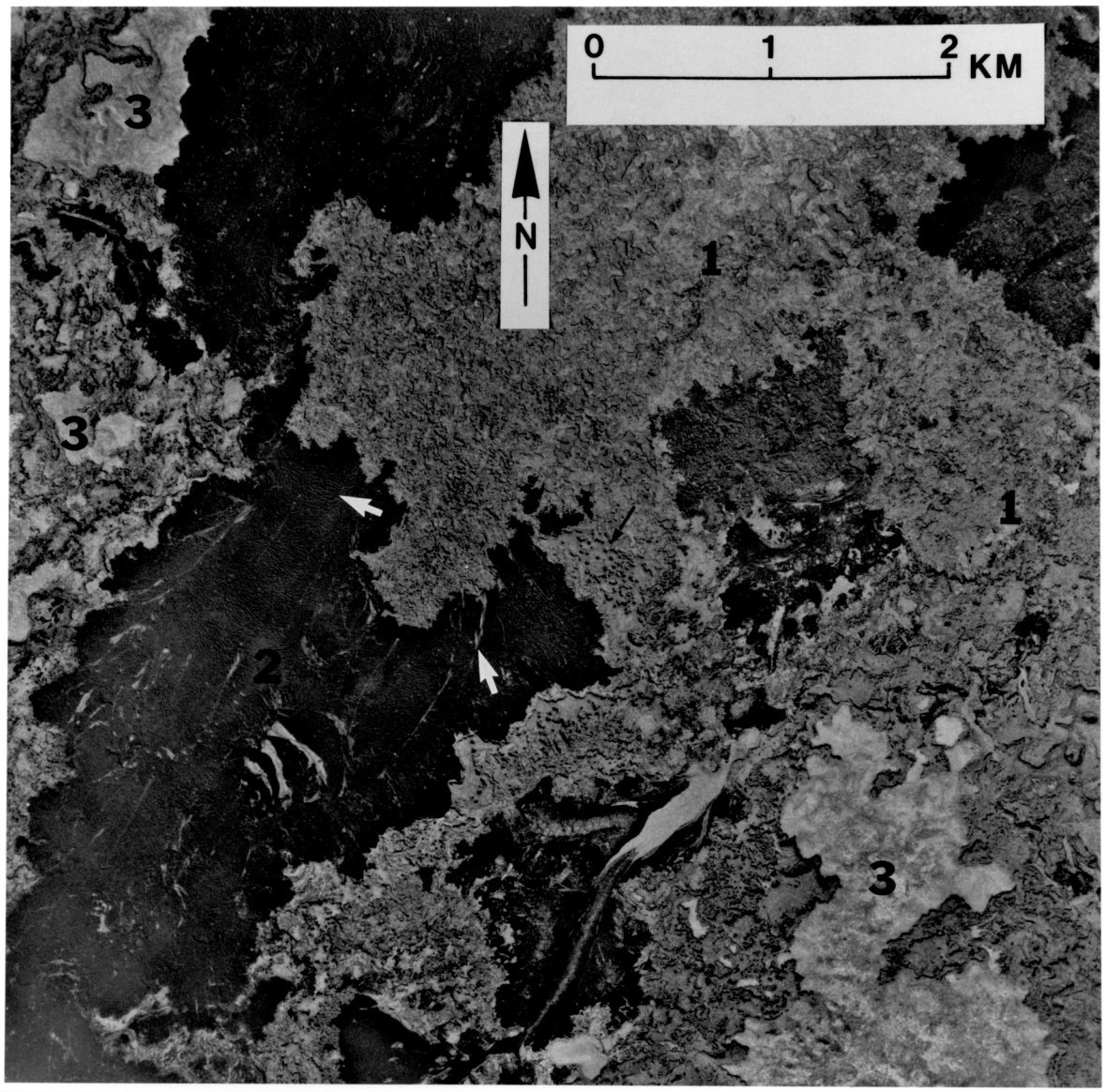

0
1
2
KM
N
3
3
1
1
2
3

Figure 15. Vertical aerial photograph of hummocky pahoehoe lava (1), aa lava (2) and smooth surfaces (3). The southern-most exposure in this scene of class 3 lava is highly weathered pahoehoe. The two class 3 exposures along the western edge of the aa flow are kipukas of Pleistocene pahoehoe covered with windblown sediments.
See Figure 13 for locations of the contacts between backscatter classes.
U.S. Geological Survey photograph, GS SWEZ 6-96, September, 1971.

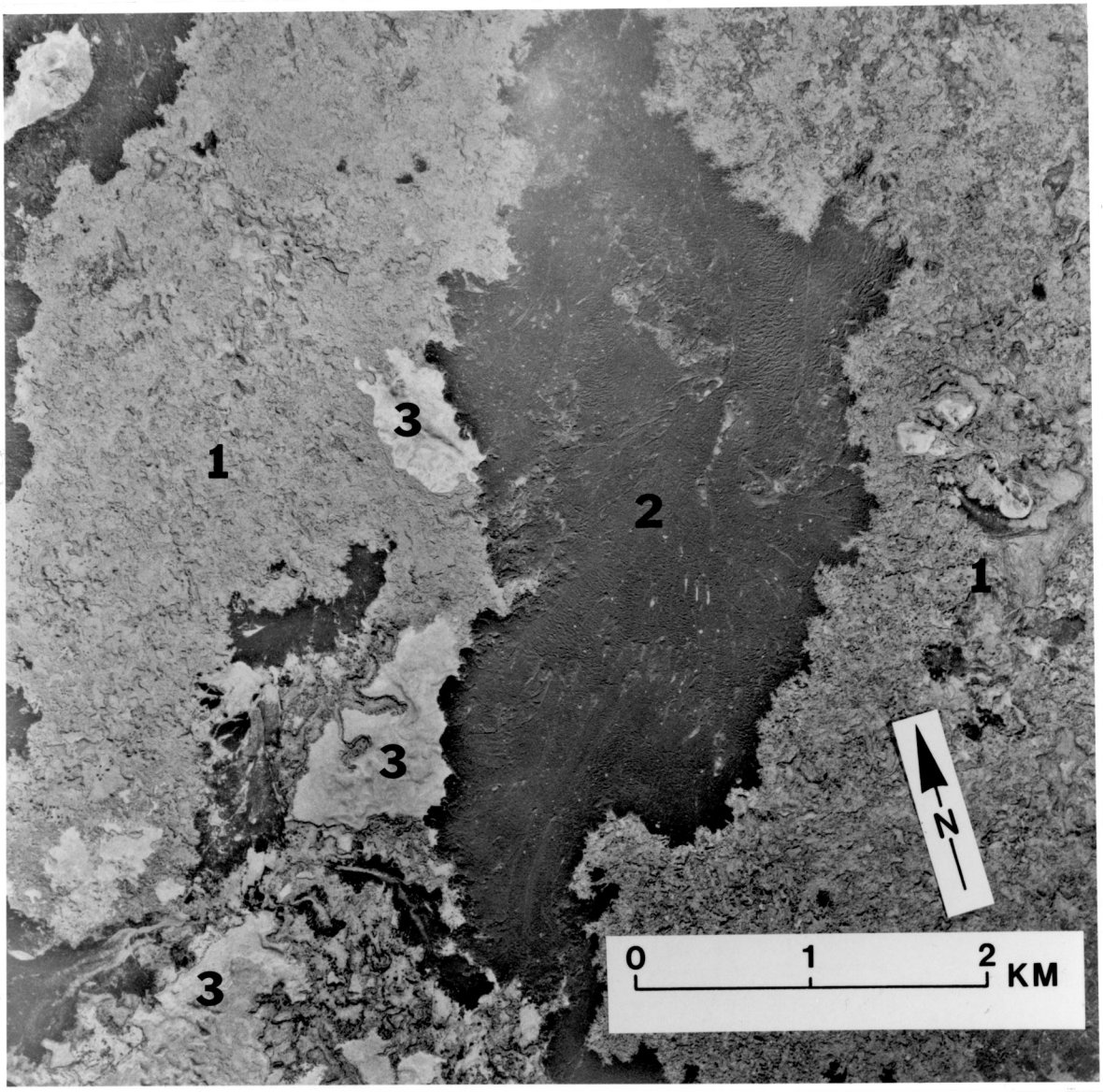

1
3
2
1
3
3
N
0
1
2
KM

Figure 16. Vertical aerial photograph of flows northwest of Black Top Butte. The butte is seen in the southeast corner (small arrow). Hummocky pahoehoe and mixed pahoehoe-aa surfaces compose class 1 flows due to similar backscatter characteristics (1). Class 3 smooth surfaces have the brightest tones (3). A 6-km-long pahoehoe flow with dark-toned aa levees trends north-south down the center of the scene (large arrow). See Figure 13 for locations of the contacts between backscatter classes. U. S. Geological Survey photograph, GS SWEZ 9-129, November, 1971.

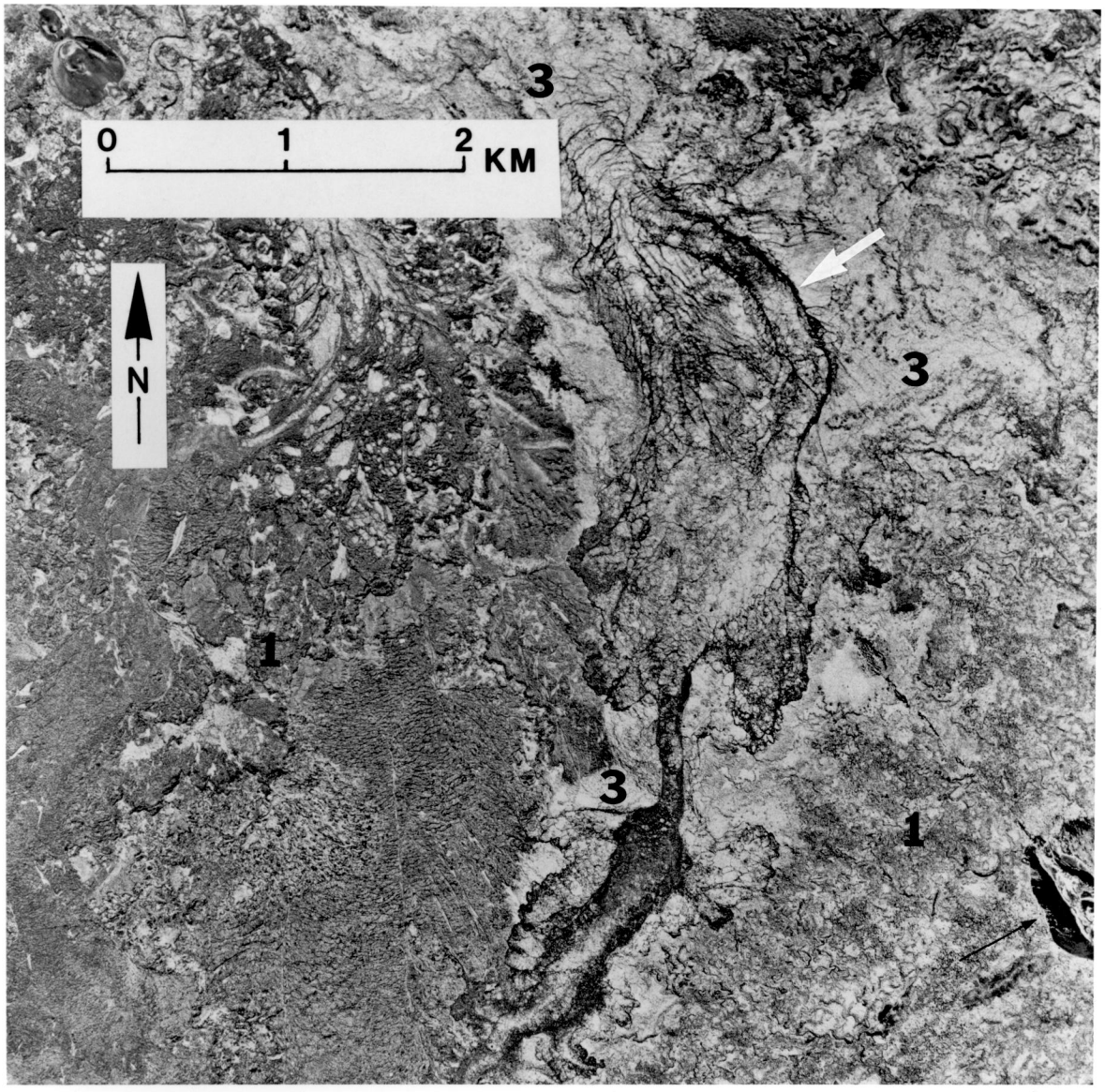
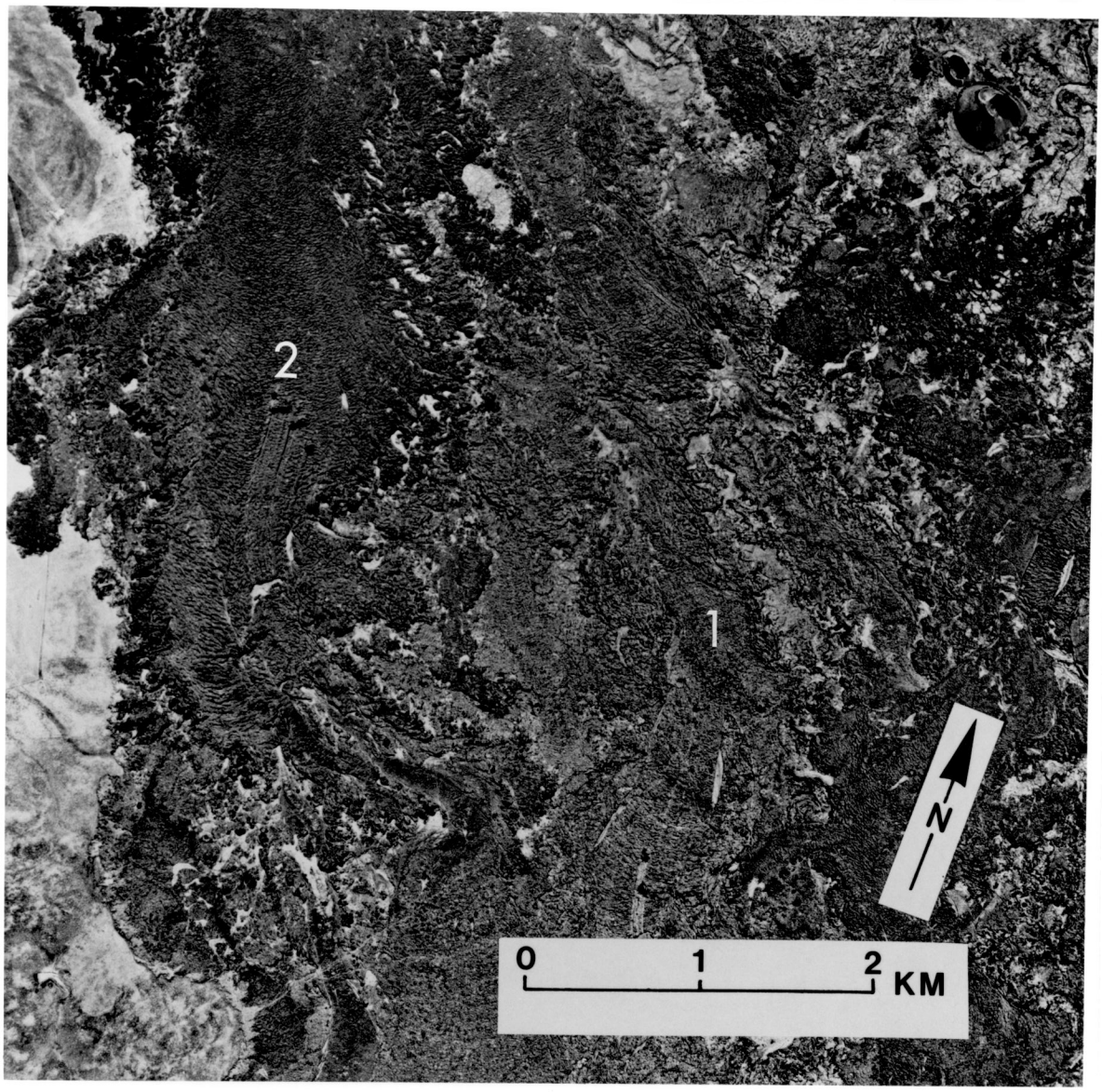

3
0 1 2 KM
N
3
1
3
1

Figure 17. Vertical aerial photograph of class 2 aa lava (2) and mixed pahoehoe-aa surfaces (1). The mixed surfaces fall into class 1 due to backscatter characteristics.
See Figure 13 for locations of the contacts between backscatter classes.
U. S. Geological Survey photograph, GS SWEZ 9-127, November, 1971.


2
1
N
0
1
2
KM

bulbous pahoehoe lobes, collapsed roofs of lava tubes, tumuli and pressure plateaus. Collapse pits in pressure plateaus near flow margins are also common (Fig. 14). Ropy pahoehoe surfaces have a micro-relief ranging from a few centimeters to a few tens of centimeters. In collapse areas surface relief of the hummocky flows generally is a few meters and locally exceeds 10 m. Hence, there is a sufficient range of surface roughness exceeding the Rayleigh criteria, for surface scattering at both X band (3 cm) and L band (25 cm) wavelengths. This accounts for the strong returns at both wavelengths and polarizations. The contributions of the aa components in the mixed pahoehoe-aa flows apparently is lorge enough to produce a strong overall return. Differences in the proportions of rough aa and smooth pahoehoe may account for the variability in backscatter from these mixed flows. It is possible that parallel-polarized returns are enhanced by resonance reflections at oblique incidence angles from slightly rough surfaces as described by the Bragg condition (Fig. 8). The horizontal spacing of pahoehoe ropes in some locations may correspond to the Bragg spatial wavelengths of approximately 2 and 20 cm at X band and L band wavelengths, respectively. Moreover, parallel-polarized returns may be supplemented by quasi-specular reflections from locally smooth faces that are longer than a radar wavelength and oriented normal to the incident energy. An example of a good reflecting surface is a broken sheet of pahoehoe which is tilted down into a collapsed tube.

Class 2 Lava Flows

The non-uniform backscatter intensity of class 2 lava flows is most influenced by radar wavelength, polarization, and surface roughness. These flows have bright tones in XHH; dark tones in XHV; bright, mottled tones in LHH and very bright tones in LHV. A range in surface roughness for these flows is interpreted to produce quasi-specular reflection of the X band (3-cm wavelength) energy and surface scattering of the L band (25-cm wavelength) energy.

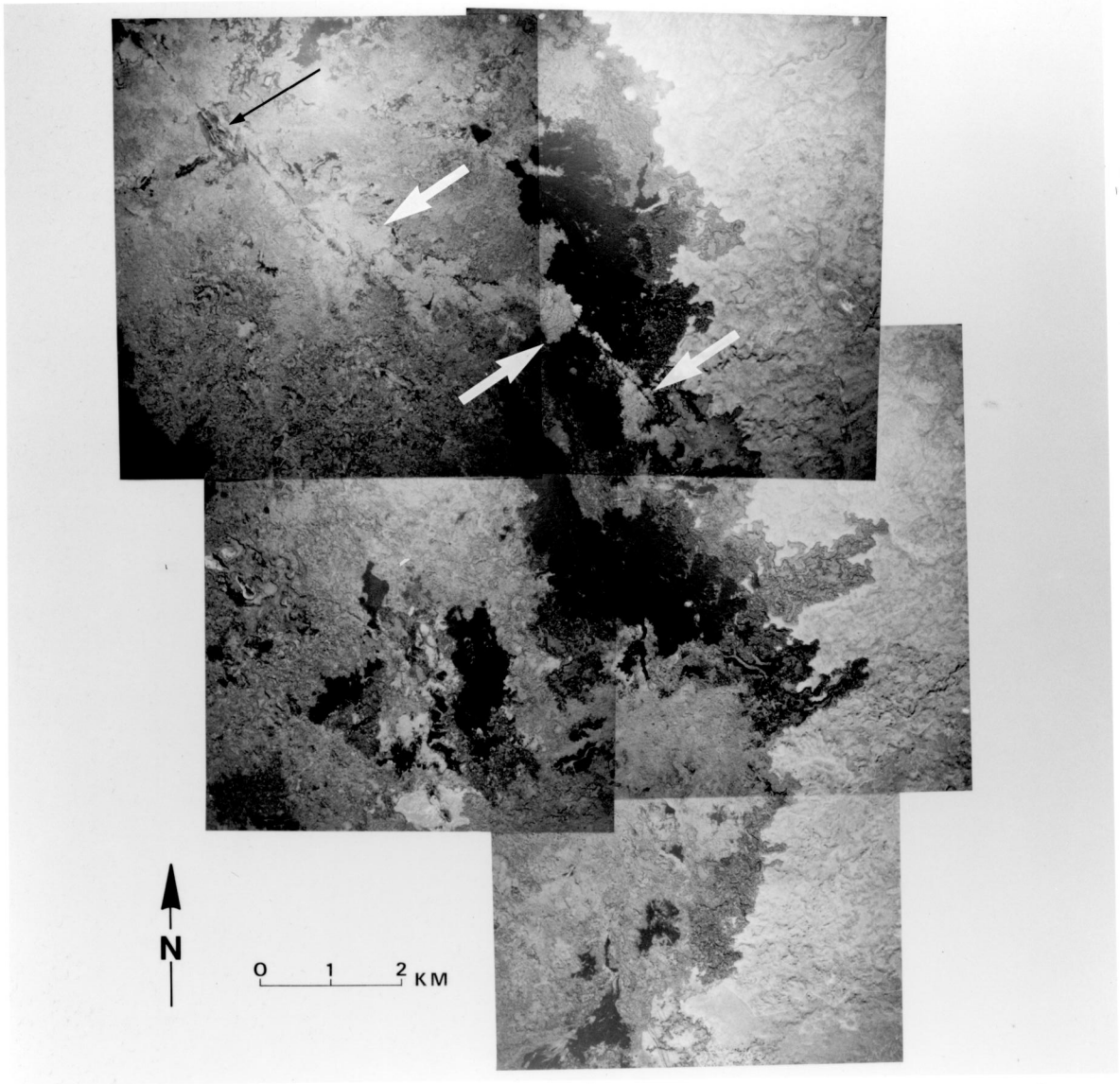
Field observations by the author show that class 2 flows are aa lava (Figs. 14,15,17,18). Surfaces locally resemble block lava because of the abundance of angular blocks. Fragments of ropy pahoehoe crust are found on the top of aa flows but are not as common as blocks. The clinkers, blocks, and fragments generally range in size from 5 to 300 cm and average 50 cm. The surface relief of the aa lava flows typically is a few tens of centimeters to a few meters. However, some flow fronts are several meters high, and some long, sinuous, V-shaped valleys in the aa flows are 4 to 5 m deep. These valleys are probably primary flow features, for their side slopes are jagged, not stream worn.

Faces of the surficial blocks and fragments are generally longer than the X band wavelength of 3 cm. The micro-roughness of these faces, whether smooth or vesicular, probably does not exceed the 1 cm Rayleigh criterion for roughness at the X band wavelength. Hence, these faces serve as good reflecting surfaces for the X band energy. Where these faces are oriented normal to the incident X band energy, strong parallel-polarized returns and weak cross-polarized returns result (Figs. 9, 10).

Figure 18. Mosaic of vertical aerial photographs of area southeast of Black Top Butte (small arrow). The Deadhorse flow (shelly pahoehoe) is the bright-toned, 8-km-long flow trending southeast (large arrows) that emanated from fissures southeast of Black Top Butte. Aa flows of class 2 are black. The rest of the scene is generally class 1 hummocky pahoehoe.

See Figure 13 for locations of the contacts between backscatter classes.

U. S. Geological Survey photographs, GS SWEZ 6-49, 6-47, 6-98, 6-100, 6-143, September, 1971.


N
0 1 2 KM

The L band (25-cm wavelength) radar energy is sensitive to the overall surface roughness of the aa flows, which exceeds the Rayleigh criterion of 3 cm at the L band wavelength. As a result, surface scattering produces strong parallel-polarized and cross-polarized returns. Parallel-polarized returns may be enhanced by Bragg resonance reflections from surface scatterers spaced 20 cm apart.

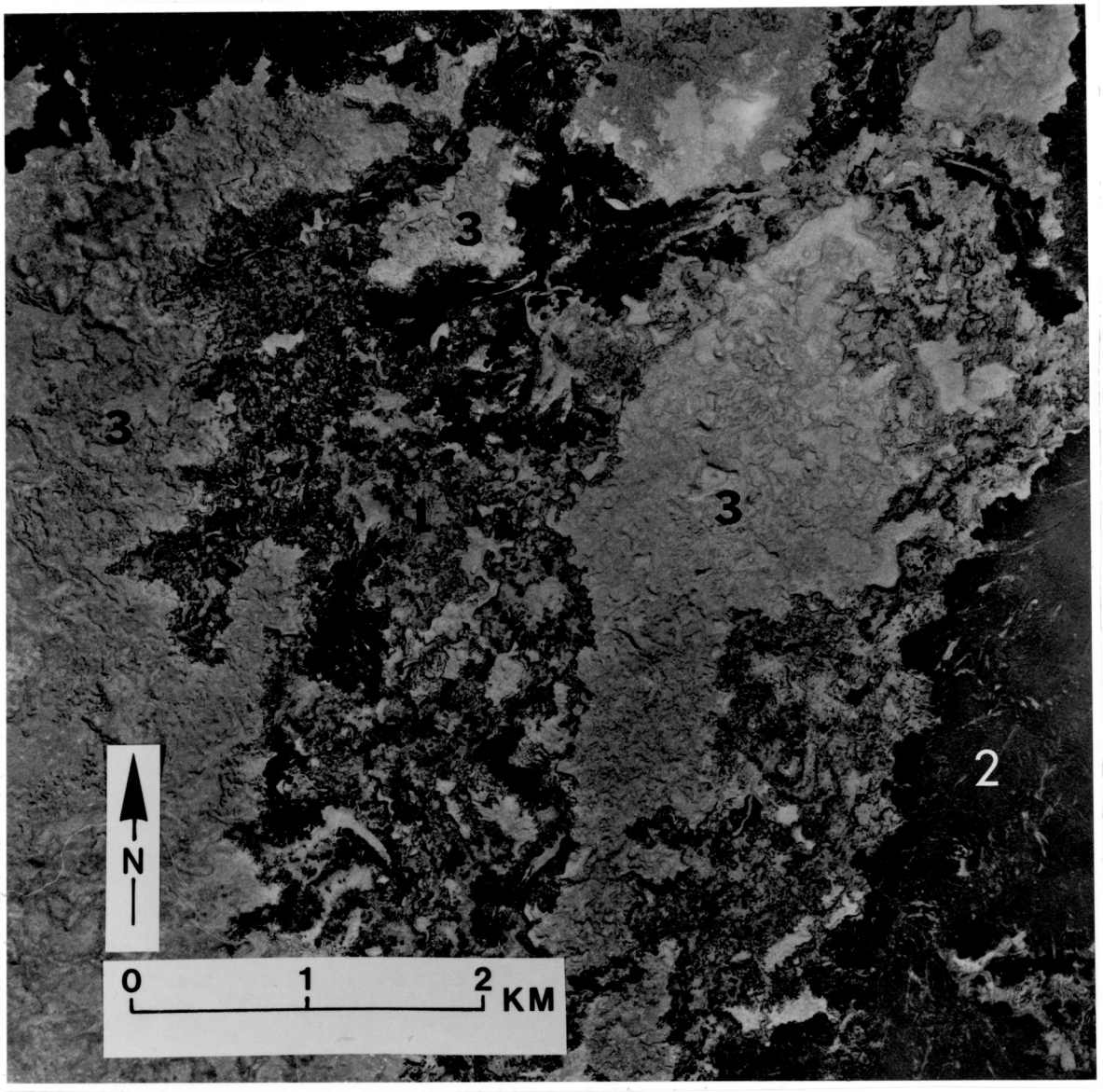
Class 1 and class 2 surfaces have similar X band parallel-polarized returns (Fig. 9) but have distinctly different X band cross-polarized signatures (Fig. 10). The locally smooth surfaces responsible for the strong HH returns in class 2 flows produce weak HV returns. The rough class 1 surfaces yield strong returns at both polarizations. Without the cross-polarized image, the two classes would be indistinguishable.

Class 3 Lava Flows

The dark tones in all four images for class 3 flows suggest that the surfaces are sufficiently smooth and flat as to reflect virtually no energy back to the radar antenna. As stated previously, rms surface heights less than 1 cm and 3 cm would appear smooth at X band and L band wavelengths, respectively.

Surface textures in this class are shelly pahoehoe, a typical near-vent texture (Fig. 18); smooth, weathered pahoehoe (Fig. 19) and pahoehoe with smooth mantles of aeolian sediments (Figs. 14, 15). The Deadhorse flow, southeast of Black Top Butte (Fig. 18) is composed of shelly pahoehoe. Field observations by the author indicate that approximately half of the surface is covered by a patchwork of rubble consisting of thin plates of pahoehoe 1 to 3 cm thick and 2 to 20 cm long. The rubble

Figure 19. Vertical aerial photograph showing exposures of class 3 weathered pahoehoe (3). Class 1 mixed pahoehoe-aa surfaces (1) and class 2 aa lava flows (2) are also shown.
See Figure 13 for locations of the contacts between backscatter classes.
U. S. Geological Survey photograph, GS SWEZ 6-148, September, 1971.


3
3
1
3
2
N
0
1
2
KM

is interpreted to be remnants of collapsed glassy blisters. The remainder of the Deadhorse flow is predominantly smooth sheets of pahoehoe. Ropy pahoehoe textures are uncommon. Surface relief of the flow generally does not exceed a few tens of centimeters, and these changes in relief occur over distnaces covering tens of meters. Scattered mounds of pahoehoe lava 10 m long and 1.5 to 2 m high occur also.

The observed surface relief exceeds the Rayleigh criteria for smooth surfaces at both radar wavelengths, yet the flow appears dark (smooth) in images at both wavelengths. This smooth appearance probably is due to variations in rms surface height occurring over ground distances substantially larger than the radar wavelengths.

Other flows with class 3 backscatter characteristics were described by Kuntz and others (1982) and include old pahoehoe flows (Figs. 3, 13) whose surface relief is subdued either becuase of extensive weathering (Fig. 19) or because of deposits of aeolian material (Figs. 14, 15). The surfaces of these flows must be approximately as smooth and flat as that of the Deadhorse flow in order to produce comparably weak returns. From the radar images one can not distinguish whether smooth surface textures are due to slight degradation, as for the collpased shelly pahoehoe, to extensive weathering or to mantling by aeolian material, as for the older pahoehoe flows.

Lava Textures Related to Vent Areas

Differences in surface textures in the lava field are displayed best in the L band, cross-polarized image (Fig. 12). From the working hypothesis, smooth textures are expected near fissure vents and surface

roughness should increase with distance from the vent. The corresponding tonal change in the image would be dark to bright. Dark-toned shelly pahoehoe flows are found near fissure vents, and an example is the Deadhorse flow that emanated from fissures southeast of Black Top Butte. However, there are other dark-toned flows in the lava field that have no direct relation to vent areas. These highly weathered or mantled pahoehoe flows have backscatter characteristics identical to those of near-vent flows. Hence, the weak backscatter of a flow does not guarentee its porximity to a fissure vent.

The hypothesis also holds that systematic textural changes from a fissure vent will occur because of the flow of lava away from the fissure. However, surface textures may be related to vent areas in complicated ways. First, flows do not always move perpendicularly from a fissure. Flows can move along the trend of the rift or at shallow angles to it resulting in different textural patterns than those expected. Second, not all flows show textural changes. Third, there may be a tendency for exposures of older lava to be distant from the vent because continued effusion may allow new flows to cover existing flows. This becomes a problem where older flows have undergone extensive weathering or are covered by windblown sediments so that the original surface texture is smoothed out. This may result in textural changes reversed from those expected away from a vent. Fourth, lava flows from off-rift sources may move toward the fissure perhaps again causing a reversal in textural transition away from the fissure. Over the entire eruptive history of a lava field, factors such as these and others are compounded and produce very complex textural patterns. The eruption scenario may be appropriate for explaining the stratigraphy of the Craters of the

Moon lava field. The textural changes of the lava field observed in the radar images are not simple transitions in single flows. Hence, it is difficult to apply the hypothesis on the scale of the entire lava field.

It may be possible to recognize pahoehoe-to-aa transitions in small, individual flows. Two flows, approximately 6 km and 2 km long, respectively, are observed in the aerial photographs (Figs. 16, 20) to have a transition in surface texture from pahoehoe to aa lava. These flows can be traced to fissure vents along the Great Rift. The 6-km-long flow has aa levees that are more apparent near the proximal end (Fig. 16). These levees can be seen in the radar images where there is a sharp contrast between textures (Fig. 12). However, the radar images do not show as clear a transition in lava textures as do the aerial photographs, perhaps due to resolution contraints. Overall, these two flows belong to class 2 because their radar backscatter resembles that from aa lava flows.

Spatter Ramparts

An en echelon pattern of bright lines in the shelly pahoehoe Deadhorse flow is seen in the X band parallel- and cross-polarized images (Figs. 9, 10). The lines match the locations of eruptive fissures and the strong backscatter is interpreted to be a result of scattering off the surface of spatter ramparts that parallel the open fissures. The spatter ramparts are several meters high and have a rough agglutinate texture (Fig. 21). The spatter ramparts are not delineated in the L band images.

Figure 20. Vertical aerial photograph showing a 2-km-long flow (bounded by arrows) with pahoehoe-to-aa textural transition. This flow emanated from a fissure in the center of this scene. The backscatter characteristics of this flow are similar to class 2 aa lava (2). Class 1 hummocky pahoehoe (1) and class 3 smooth surfaces (3) are also shown. See Figure 13 for locations of the contacts between backscatter classes. U. S. Geological Survey photograph, GS SWEZ 9-190, November, 1971.

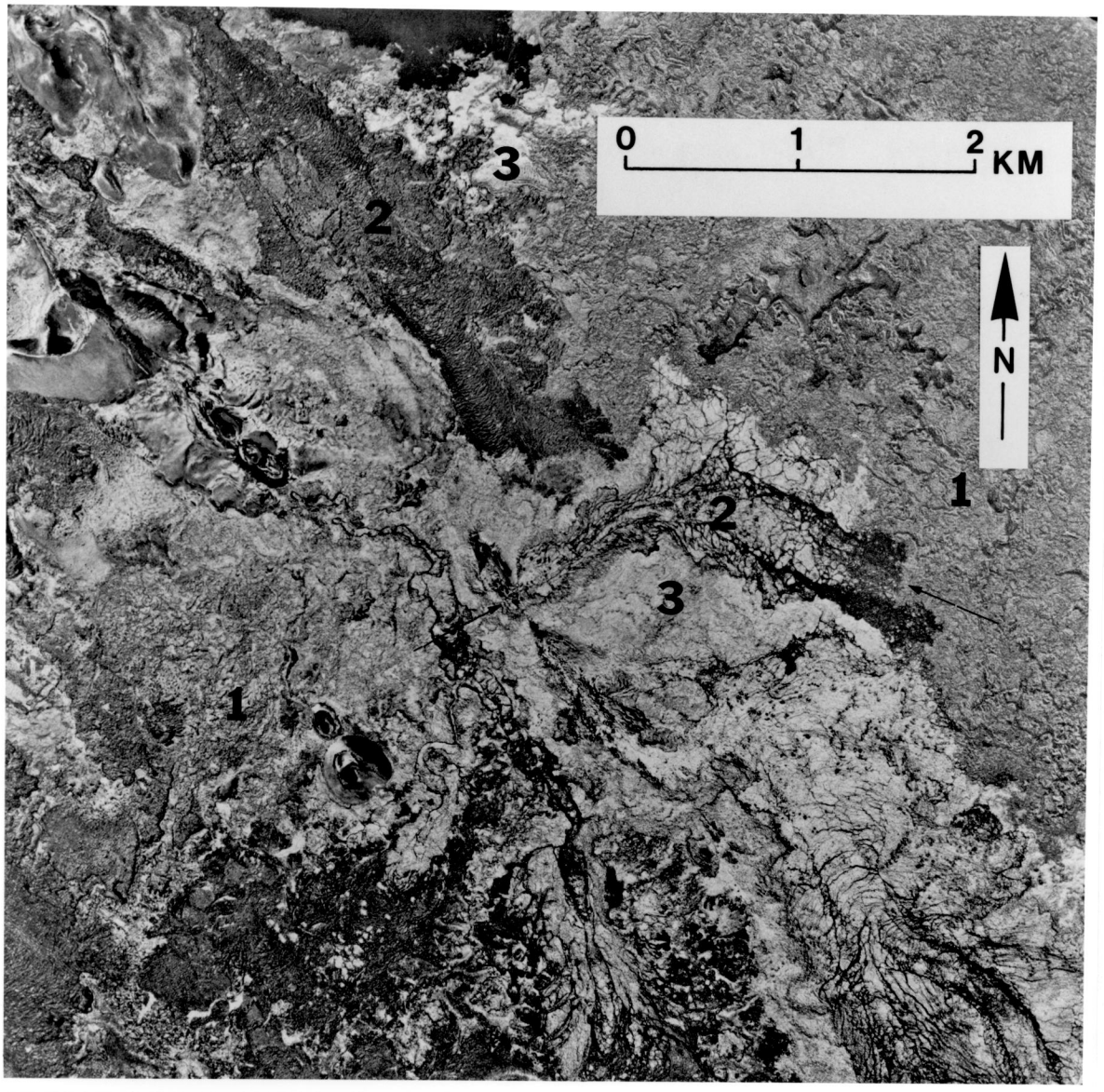

0
1
2
KM
N
3
2
1
2
3
1



Figure 21. Ground photograph of spatter ramparts paralleling open fissures in the Deadhorse flow, southeast of Black Top Butte. Rampart on the right is several meters high. View is to the southeast.

Considering the importance of spatter ramparts as vent indicators it is critical to attempt to explain why they are only detected in the X band images. The clots of agglutinate spatter give the rampart surfaces a micro-relief of several centimeters. This surface roughness is more likely to cuase scattering of the X band energy than of the longer wavelength L band energy. Although the structures can be several meters high the look directions for both imaging systems are approximatley parallel to the trend of the ramparts, so the walls do not serve as reflectors. This emphasizes the importance of look direction in detecting potential reflectors. It is also possible that system designs governing resolution, such as transmitted power, antenna gain, sensitivity to temperature, number of looks, and signal to noise ratio may contribute to the difference in visibility of the spatter ramparts in the radar images. It is not possible at this time to unequivocally isolate the most important contributing factor.

CONCLUSIONS

One of the major objectives of this project has been to determine whether textural changes in basaltic lava flows can be identified in radar images and used to locate fissure vents. Smooth and rough surface textures of basaltic lava flows in the Craters of the Moon (COM) lava field can be successfully distinguished in X band (3 cm wavelength) and L band (25 cm wavelength), dual polarizations images. However, there are limitations in using textural changes to locate fissure vent areas. Two major constraints are difficulties in differentiating smooth, near-vent flows from other types of smooth surfaces, and difficulties in tracing smooth to rough textural transitions back to a particular vent area.

Shelly pahoehoe lava and older pahoehoe lava flows, some of which have smooth mantles of aeolian material, have identical backscatter characteristics. Hence, weak backscatter is not diagnostic of a near-vent flow.

The stratigraphy of the lava field also places constraints on relating surface textures to fissure vent areas. Textural transitions seen in the radar images generally did not result from single flows of lava emanating from fissure vents. Rather, lavas of different textures, degrees of weathering, flow paths, and source vents combined to form complex textural patterns. In stratigraphically complex fields it is difficult to associate systematic textural changes with a particular vent area. The hypothesis that vent areas can be recognized by smooth to rough textural changes in the effused lavas is therefore difficult to apply on the scale of the entire lava field. Some individual flows do

show such textural transitions. However, due to resolution limitations, the radar images generally did not show these transitions clearly.

Another objective of this project was to determine if fissure vents themselves or vent structures could be located in the radar images. Eruptive fissures are detectable in the radar images by virtue of the structures that form along their length. Spatter ramparts paralleling the eruptive fissures have diagnostic, strong backscatter in the X band images that contrasts with the weak backscatter of the surrounding shelly pahoehoe lava. Spatter ramparts in the Deadhorse flow are particularly well defined. However, such structures do not always form, and they can be destroyed by the continued effusion of lava. Therefore, searches for vent structures may not be a universally successful means of locating eruptive fissures.

Spatter ramparts were not delineated in the L band images. The agglutinate texture of the ramparts is several centimeters, which may not be sufficient to cause scatter of the L band energy. Resolution differences between the radar systems may also account for the appearance of spatter ramparts only in the X band images. The issue of spatter rampart visibility illustrates well the significance of using multiple wavelengths in radar studies.

Additional work suggested by the results of this study include more detailed field studies of the surface roughness of the lava flows, and more detailed studies of radar signatures of lava textures. Also, a better understanding of the effects of vegetation on radar backscatter is warranted, although the backscatter characteristics of the Craters of the Moon flows could be explained fully by the lava textures.

REFERENCES CITED

Beckmann, P., and Spizzichino, A., 1963, Electromagnetic Scattering From Rough Surfaces: New York, MacMillian, 503 p.

Daily, M., Elachi, C., Farr, T., Stromberg, W., Williams, S., and Schaber, G., 1978, Application of multispectral radar and Landsat imagery to geologic mapping in Death Valley: Jet Propulsion Laboratory Publication 78-19, 47 p.

Daily, M., Blom, R., Elachi, C., and Saunders, R. S., 1979, Analysis of the radar imagery of the eastern Snake River Plain: National Aeronautics and Space Administration Technical Memorandum 80339, p. 362-364.

Dellwig, L. F., 1969, An evaluation of multifrequency radar imagery of the Pisgah Crater area, California: Modern Geology, v. 1, p. 65-73.

Dellwig, L. F., and Moore, R. K., 1966, The geologic value of simutaneously produced like- and cross-polarized radar imagery: Journal of Geophysical Research, V. 71, p. 3597-3601.

Elachi, C., Blom, R., Daily, M., Farr, T., and Saunders, R. S., 1980, Radar imaging of volcanic fields and sand dune fields: Implications for VOIR, in Radar Geology: An Assessment, Report of the Radar Geology Workship, Snowmass, Colorado, Jet Propulsion Laboratory Publication 80-61, p. 114-150.

Evans, D. L., 1978, Radar observations of a volcanic terrain: Askja caldera, Iceland: Jet Propulsion Laboratory Publication 78-81, 39 p.

Farr, T., Elachi, C., Daily, M., and Blom, R., 1981, Imaging radar observations of volcanic features in Medicine Lake Highland, California, in Carver, K.R., ed., IEEE International Geoscience and Remote Sensing Symposium Digest, p. 872-877.

Fung, A. K., and Ulaby, F. T., 1983, Matter-energy interaction in the microwave region, in Simonett, D. S., and Ulaby, F. T., eds., Manual of Remote Sensing, 2nd ed., p. 115-164.

Greeley, R., 1982, The Snake River Plain, Idaho: Representative of a new category of volcanism: Journal of Geophysical Research, v. 87, p. 2705-2712.

Janza, F. T., 1975, Interaction mechanisms, in Janza, F. T., Blue, H., and Johnston, J. E., eds., Manual of Remote Sensing, 1st ed., p. 75-179.

Kuntz, M. A., Champion, D. E., Spiker, E. C., Lefebvre, R. H., and McBroome, L. A., 1982, The Great Rift and the evolution of the Craters of the Moon lava field, Idaho, in Bonnichsen, B., and Breckenridge, R. M., eds., Cenozoic Geology of Idaho, Idaho Bureau of Mines and Geology, bulletin 26, p. 423-437.

Kuntz, M. A., Mabey, D. R., Champion, D. E., Stanley, W. D., Lefebvre, R. H., Spiker, E. C., McBroome, L. A., and Covington, H. R., 1983, Geologic and geophysical maps of the Great Rift instant study area, Blaine, Butte, Minidoka, and Power Counties, Idaho: U. S. Geological Survey Miscellaneous Field Studies Map MF-1462-A, scale 1:125,000, 2 sheets.

Leeman, W. P., Vitaliano, C. J., and Prinz, M., 1976, Evolved lavas from the Snake River Plain: Craters of the Moon National Monument, Idaho: Contributions to Mineralogy and Petrology, v. 56, p. 35-60.

Long, M. W., 1975, Radar Reflectivity of Land and Sea: Lexington, D. C. Heath and Company, 366 p.

Macdonald, G. A., 1973, Volcanoes: Englewood Cliffs, Prentice-Hall, Inc., 510 p.

Malin, M. C., Evans, D., and Elachi, C., 1978, Imaging radar observations of Askja Caldera, Iceland: Geophysical Research Letters, v. 5, p. 931-934.

Prinz, M., 1970, Idaho Rift System, Snake River Plain, Idaho: Geological Society of America Bulletin, v. 81, p. 941-948.

Sabins, F. F., Jr., 1978, Remote Sensing Principles and Interpretation: San Francisco, W. H. Freeman and Company, 426 p.

Schaber, G. G., Elachi, C., and Farr. T. G., 1980, Remote sensing data of SP Mountain and SP lava flow in north-central Arizona: Remote Sensing of Environment, v. 9, p. 149-170.

Stone, G. T., 1967, Petrology of Upper Cenozoic basalts of the Snake River Plain [Ph.D. thesis]: Boulder, Colorado, University of Colorado, 392 p.

Stout, M. Z., and Nicholls, J., 1977, Mineralogy and petrology of Quaternary lavas from the Snake River Plain, Idaho: Canadian Journal of Earth Sciences, v. 14, p. 2140-2156.

Swanson, D. A., 1973, Pahoehoe flows from the 1969-1971 Mauna Ulu eruption, Kilauea Volcano, Hawaii: Geological Society of America Bulletin, v. 84, p. 615-626.

Ulaby, F. T., Moore, R. K., and Fung, A. K., 1982, Microwave Remote Sensing Active and Passive, v. 2, Radar Remote Sensing and Surface Scattering and Emission Theory: Reading, Addison-Wesley Publishing Company, 1064 p.